JCI The Journal of Clinical Investigation

Repression of rRNA gene transcription by endothelial SPEN deficiency normalizes tumor vasculature via nucleolar stress

Zi-Yan Yang, … , Tian Xiao, Hua Han

J Clin Invest. 2023. https://doi.org/10.1172/JCI159860.

Research In-Press Preview Vascular biology

Graphical abstract

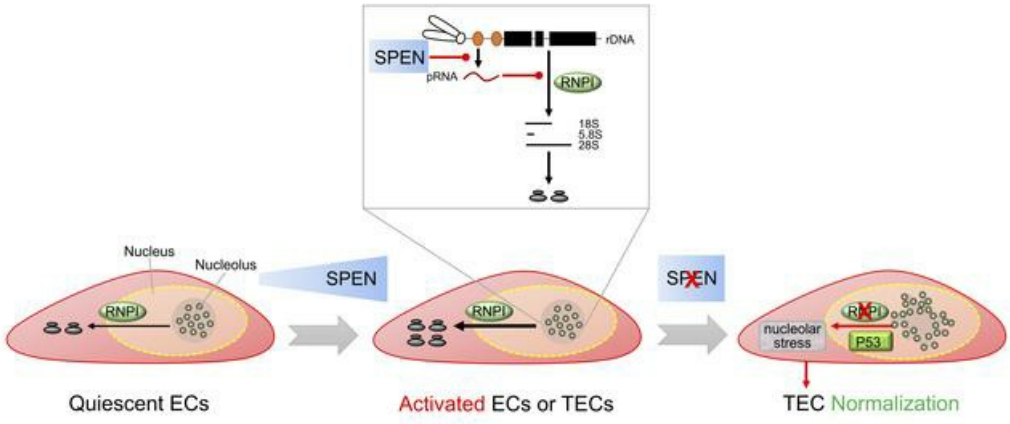

Repression of rRNA gene transcription by endothelial SPEN deficiency normalizes tumor vasculature via nucleolar stress

Zi-Yan Yang, Xian-Chun Yan, Jia-Yu-Lin Zhang, Liang Liang, Chun-Chen Gao, Pei-Ran Zhang, Yuan Liu, Jia-Xing Sun, Bai Ruan, Juan-Li Duan, Ruo-Nan Wang, Xing-Xing Feng, Bo Che, Tian Xiao, Hua Han*

State Key Laboratory of Cancer Biology, Department of Biochemistry and Molecular Biology, Fourth Military Medical University, Xi'an 710032, China

*Corresponding author: Hua Han, Department of Biochemistry and Molecular Biology, Fourth Military Medical University, Chang-Le Xi Street #169, Xi'an 710032, China, Tel, FAX, +86-029-83246270, email, huahan@fmmu.edu.cn.

Authorship note: YZY, YXC, and ZJYL share first authorship.

Abstract

Human cancers induce a chaotic, dysfunctional vasculature that promotes tumor growth and dampens most current therapies, but the underlying mechanism has been unclear. Here we show that SPEN (*split end*), a transcription repressor, coordinates ribosome RNA (rRNA) synthesis in endothelial cells (ECs) and is required for physiological and tumor angiogenesis. SPEN deficiency attenuated EC proliferation and blunted retinal angiogenesis, which was attributed to p53 activation. Furthermore, SPEN knockdown activated p53 by upregulating the noncoding promoter RNA (pRNA), which represses rRNA transcription and triggers p53-mediated nucleolar stress. In human cancer biopsies, low endothelial SPEN level correlated with extended overall survival. Consistently in mice, endothelial SPEN deficiency compromised rRNA expression and repressed tumor growth and metastasis by normalizing tumor vessels, which was abrogated by p53 haploinsufficiency. rRNA gene transcription is driven by RNA polymerase I (RNPI). We found that CX-5461, an RNPI inhibitor, recapitulated the effect of *Spen* ablation on tumor vessel normalization, and combining CX-5461 with cisplatin substantially improved the efficacy on treating tumors in mice. Together, these results demonstrate that SPEN is required for angiogenesis by repressing pRNA to enable rRNA gene transcription and ribosomal biogenesis, and that RNPI represents a target for tumor vessel normalization therapy of cancer.

Key words: SPEN, rDNA, nucleolar stress, pRNA, endothelial cells, tumor vessels

Introduction

Angiogenesis, the growth of new vessels from existing ones, is required for vascularization of both physiological and pathological tissues (1). Tumor angiogenesis, however, is driven by abnormally high level of proangiogenic factors to thereby form a prosperous but chaotic vasculature characterized by disordered morphology, hyper-activated endothelial cells (ECs), and reduced pericyte and basement membrane coverage, leading to enhanced hypoxia and vessel leakage (2). The tumor vasculature promotes tumor growth and metastasis and blunts most current therapies. Anti-angiogenesis therapy (AAT) normalizes chaotic tumor vessel structures and functions to compromise tumor malignancy and facilitate other therapies (3–5). To date, cytokines, signal transduction and gene expression regulators, and metabolic enzymes have been tested as AAT targets (3, 4, 6). However, the efficacy of current AATs appears not satisfying in at least some cancers and resistance often emerges early, prompting discovering new AAT targets (7, 8).

Recent single-cell RNA-sequencing (scRNA-seq) studies have revealed that ECs contain heterogeneous subsets with distinct proliferation, differentiation, and metabolic characteristics (9–11). Of note, compared with quiescent ECs, activated ECs, including tumor ECs (TECs), in angiogenesis exhibit higher expression of ribosome-related genes, implying that ribosome biogenesis is required for angiogenesis (9–11). Ribosomes are composed of ribosomal proteins (RPs) and ribosomal (r)RNAs (12, 13). The 18S, 5.8S, and 28S rRNAs are encoded by the ribosomal DNA (rDNA) and transcribed as a pre-rRNA by RNA polymerase I (RNPI) in nucleoli (14, 15). Extrinsic and intrinsic insults

disrupting balanced ribosomal biogenesis interrupt the murine double minute (MDM) 2-p53 interaction, resulting in p53-mediated nucleolar stress, which is characterized by decreased ribosome biogenesis, deformed nucleolar morphology, and cell cycle arrest (16–18). So far, the role of ribosome biogenesis in angiogenesis remains unclear.

Split end (SPEN, or SMRT/HDAC1-associated repressor protein [SHARP] in humans and Msx2-interacting nuclear target protein [MINT] in mice) is an ~400 kDa large RNA-binding transcription repressor with a C-terminal SPEN paralogue and orthologue C-terminal (SPOC) domain (19, 20). SPEN negatively regulates several signalling pathways, such as Notch (21, 22). SPEN also plays an essential role in X-chromosome inactivation by associating with X inactive specific transcript (XIST) and recruiting histone modification enzymes via the SPOC domain (23, 24). In addition, SPEN associates with the lncRNA steroid receptor RNA activator (SRA) that binds CCCTC-binding factor (CTCF) (20, 25), and participates in silencing endogenous retroviruses (26). SPEN deficient mice are embryonic lethal, accompanied by multiple developmental disorders in their liver, pancreas, brain, and haematopoietic system (22), suggesting that SPEN plays a critical role in development. However, the role of SPEN in angiogenesis has not been elucidated. In this study, we demonstrate that SPEN is required for angiogenesis by enabling efficient rRNA transcription driven by RNPI. Endothelial SPEN deficiency, and the RNPI inhibitor CX-5461 (27–30) as well, represses tumor growth via tumor vessel normalization. Therefore, the ribosome biogenesis machinery is a druggable target for AAT of human cancers.

Results

83 **SPEN knockdown arrests EC proliferation and blunts angiogenesis.**
84 Immunofluorescence of mouse tissue sections showed that SPEN is expressed in ECs
85 (Supplemental Figure 1A). In human umbilical vein endothelial cells (HUVECs),
86 SPEN was detected exclusively in nuclei (Supplemental Figure 1B). To investigate the
87 role of SPEN in ECs, we transduced HUVECs with lentivirus expressing a *SPEN*
88 shRNA (shRNA2, named as SPENi hereafter, Supplemental Figure 1, C and D) or its
89 nonsense control (NC). SPEN knockdown resulted in reduced proliferation of HUVECs
90 as shown by EdU incorporation and cell cycle analysis (Figure 1, A and B). Live cell
91 imaging showed that SPEN knockdown led to cell division arrest accompanied by
92 enlarged cell size, and cell migration was mildly reduced (Figure 1C, Supplemental
93 Video, 1 and 2 and Supplemental Figure 1, E and F). We performed RNA-seq of
94 HUVECs transduced with SPENi or NC lentivirus, and analysed data by principal
95 component analysis (PCA) (Supplemental Figure 1G). The result confirmed the
96 downregulation of cell cycle-related genes in HUVECs with SPEN knockdown (Figure
97 1D and Supplemental Figure 1H). These data demonstrate that SPEN is required for EC
98 proliferation.
99 Angiogenesis-associated genes, including ETS proto-oncogene 1 (*ETS1*),
100 connective tissue growth factor (*CTGF*), angiopoietin 2 (*ANGPT2*), *VEGFR2*, and
101 heparan sulfate proteoglycan 2 (*HSPG2*), were downregulated in HUVECs with SPEN
102 knockdown, as confirmed by RT–qPCR, immunoblotting and immunofluorescence
103 (Figure 1, E and F and Supplemental Figure 1, I and J). Consistently, the in vitro
104 sprouting assay showed that SPEN knockdown compromised HUVEC sprouting

105 (Figure 1G). To determine the role of SPEN in angiogenesis in vivo, we induced EC-
106 specific *Spen* ablation in *Cdh5-Cre*^{ERT2}-*Spen*$^{f/f}$ (e*Spen* $^{-/-}$) postnatal day (P) 1 pups and
107 adult mice using tamoxifen (Supplemental Figure 2, A–E) (31). On P6, retinal whole-
108 mount CD31 staining showed that while the radius of the retinal vasculature did not
109 change, EC areas, vessel branch points, and distal vessel sprouts decreased, with some
110 micro-vessels appearing "broken" in e*Spen* $^{-/-}$ pups (Figure 1H). A Matrigel plug assay
111 showed that while the Matrigel plugs were well vascularized on day 7 in the control,
112 vascularization was almost blocked in e*Spen* $^{-/-}$ mice (Supplemental Figure 2F). EdU
113 incorporation and Ki67 staining also showed that *Spen* ablation resulted in reduced EC
114 proliferation (Figure 1I and Supplemental Figure 2, G and H). Together, these results
115 indicate that endothelial SPEN is required for angiogenesis by supporting EC
116 proliferation.

117 **SPEN knockdown arrests EC proliferation via p53.** Gene expression profiling
118 revealed that p53 signalling was remarkably upregulated in HUVECs with SPEN
119 knockdown (Figure 2A and Supplemental Figure 3A) (32). RT–qPCR and
120 immunoblotting confirmed that p53 downstream molecules, including *p21* and growth
121 arrest and DNA damage inducible alpha (*GADD45A*), were upregulated in HUVECs
122 with SPEN knockdown, while p53 was upregulated at the protein but not the mRNA
123 level (Figure 2, B and C). Further analyses showed that nuclear p53 increased
124 accompanied by increased transactivation activity, as shown by immunoblotting and
125 reporter assay, respectively (Supplemental Figure 3, B and C). The p53 protein level is
126 predominantly regulated by MDM2, which prevents proteasome-mediated p53

127 degradation via protein-protein interaction (32, 33). We treated HUVECs transduced
128 with SPENi or NC with cycloheximide (CHX) and monitored p53 level by
129 immunoblotting. The result showed that SPEN knockdown delayed the decrease of p53
130 and prolonged its half-life, suggesting inhibited degradation, while MDM2 degradation
131 appeared unaltered (Figure 2, D–F and Supplemental Figure 3D). Consistently, p53-
132 associated MDM2 decreased in SPENi-transfected HUVECs, as determined by
133 immunoprecipitation (Figure 2G). These results suggest that SPEN knockdown in ECs
134 results in p53 activation by delayed degradation.

135 To assess the role of p53 in the SPEN knockdown-induced proliferation arrest in
136 ECs, we transduced HUVECs with SPENi together with a lentivirus expressing *p53*
137 shRNA (p53i). p53 knockdown abrogated the upregulation of p21 and GADD45A in
138 HUVECs transfected with SPENi (Figure 3A). Consequently, p53 knockdown
139 ameliorated the SPENi-induced proliferation arrest, cell size enlargement, and
140 sprouting defects, as determined by EdU incorporation, live cell imaging, and sprouting
141 assay, respectively (Figure 3B). Cell cycle analysis confirmed that p53 knockdown
142 rescued SPENi-induced G1 arrest (Figure 3C). Knockdown of p21 with shRNA (p21i)
143 showed similar effects (Supplemental Figure 3, E–G). We also transduced HUVECs
144 with SPENi or NC, and a MDM2 overexpression lentivirus simultaneously. The result
145 showed that overexpressing MDM2 rescued p21 expression and cell proliferation
146 (Figure 3, D–F and Supplemental Figure 3, H–J). These results indicate that SPEN
147 knockdown represses EC proliferation by activating p53.

148 **SPEN knockdown upregulates pRNA to thereby downregulate pre-rRNA**
149 **transcription, leading to nucleolar stress activating p53.** Next, we set out to
150 determine the mechanism underlying p53 activation in ECs with SPEN knockdown.
151 We examined Ser15, Ser20 and Thr18 phosphorylation of p53, which is involved in
152 p53-MDM2 interaction and activation (34, 35), by immunoblotting. The result showed
153 that SPEN knockdown did not change p53 phosphorylation at these residues
154 remarkably (Supplemental Figure 3K). PIN1, a peptidyl-prolyl cis-trans isomerase
155 binding to Thr81-phosphorylated p53 to thereby prevent p53-MDM2 interaction (36,
156 37), was downregulated in HUVECs with SPEN knockdown (Supplemental Figure 3L).
157 Therefore, p53 upregulation might not be resulted from altered phosphorylation.
158 RNA-seq showed that the ribosome-related genes were downregulated in HUVECs
159 with SPEN knockdown (Figure 2A). Ribosomes are generated in nucleoli, phase-
160 separated, membrane-less organelles with a fibrillar centre (FC) surrounded by a dense
161 fibrillar component (DFC) layer and an outside granular component (GC) layer (16, 17,
162 38). Disturbed ribosomal biogenesis leads to p53 activation by disrupting the MDM2-
163 p53 interaction, a process called nucleolar stress (16–18). In HUVECs, SPEN
164 knockdown resulted in irregularly shaped nucleoli that unraveled throughout the
165 nucleoplasm in dispersed fibrillar structures, in contrast to round and regular nucleoli
166 in the control (Figure 4A). Immunostaining of the nucleolar markers RPA40 (FC), FBL
167 (DFC), and NPM1 (GC) followed by structured illumination microscopy (SIM)
168 confirmed that although SPEN appeared not in nucleoli, SPEN knockdown resulted in
169 the fusion of nucleoli, where the FC and DFC regions relocated to the nucleolar

170 periphery and surrounded the remnant GC, appearing as unraveled "nucleolar necklaces"
171 (Figure 4, B and C and Supplemental Figure 4A) (17). Quantitative analyses showed
172 that, in contrast to the control, the FC and DFC markers were distributed outside the
173 GC area in SPEN knockdown HUVECs, leading to deformed nucleoli (Figure 4, B–D).
174 Functionally, the RP gene expression was downregulated in HUVECs with SPEN
175 knockdown (Figure 4, E–G). Moreover, in SPENi-transfected HUVECs, MDM2-bound
176 RPL5 and RPL11, as well as 5S rRNA, increased markedly, suggesting that SPEN
177 knockdown increased MDM2 associated with ribosomal proteins in the form of
178 ribonucleoprotein particle (RNP) containing RPL5, RPL11, and 5S rRNA (Figure 4H)
179 (16–18). These results demonstrate that SPEN is required for maintaining the nucleolar
180 structure and function in ECs, and SPEN deficiency tiggers nucleolar stress to thereby
181 activate p53 in ECs.

182 We further explored how SPEN deficiency impaired ribosome biogenesis in ECs.
183 NPM1 sustains nucleolar organization (39). However, the NPM1 protein level was not
184 influenced by SPEN knockdown (Supplemental Figure 4B). In human and mouse,
185 approximately 300 rDNA copies per haploid genome are arranged as tandem repeats on
186 the short arms of acrocentric chromosomes (14, 15, 38). Each rDNA unit is divided into
187 an ~13 kb pre-rRNA-encoding gene and an ~30 kb intergenic spacer (IGS) region,
188 which contains an rRNA gene promoter proximal to and responsible for pre-rRNA gene
189 transcription and an upstream spacer promoter that enhances the gene promoter (14, 15,
190 40–42). We found that pre-rRNA and processed 18S, 5.8S and 28S rRNAs were

191 downregulated in SPENi-transfected HUVECs (Figure 5A), suggesting that SPEN
192 knockdown downregulates rRNA gene expression, leading to nucleolar stress (16–18).
193 RNPI-mediated rDNA transcription is controlled at several levels. Histone
194 modifications, histone exchange, and the upstream binding factor (UBF)-mediated
195 nucleosome replacement epigenetically regulate rDNA, while preinitiation complex
196 assembly requires CTCF, DNA isomerases, and cohesin/condensin complexes (14, 15,
197 43–45). Moreover, at least three noncoding (nc)RNAs regulate rRNA gene transcription
198 (Supplemental Figure 4C) (46–50): RNPI-driven promoter RNA (pRNA) silences pre-
199 rRNA genes on inactive rDNA loci; stress-induced promoter and pre-rRNA antisense
200 RNA (PAPAS) is transcribed by RNPII from the IGS in the antisense direction and
201 inhibits pre-rRNA gene transcription; and IGS-derived sense and antisense ncRNAs
202 regulate rRNA transcription via R-loop formation. We examined RNPI and UBF
203 uploading as well as histone modifications around the promoter region of the rDNA
204 repeats by ChIP-qPCR (44). RNPI and UBF binding was markedly decreased around
205 the gene promoter of rDNA repeats, accompanied by decreased activation (H3K4me2,
206 H2A.Z, H3ac) and increased repression histone marks (H3K27me3, H4K20me3)
207 (Figure 5B). RNPI recruitment is dependent on CTCF, which associates with lncRNA
208 SRA that binds SPEN (20, 25). However, the binding of CTCF to rDNA was not
209 changed (Figure 5B), and in our hand, overexpressing CTCF did not upregulate pre-
210 rRNA in HUVECs (Supplemental Figure 4D). Next, by using strand-specific RT–qPCR,
211 we found that the IGS transcripts from both sense and antisense chains were not altered
212 after SPENi transfection (Supplemental Figure 4E). Similarly, the PAPAS level was

213 comparable between SPENi- and NC-transfected HUVECs (Supplemental Figure 4F).
214 Finally, chain-specific RT–qPCR showed that the pRNA level increased substantially
215 in SPENi-transfected HUVECs (Figure 5C), suggesting that SPEN knockdown in ECs
216 results in disrupted nucleolar structure and functions likely via the upregulated pRNA.

217 We also evaluated *Spen* knockout-induced nucleolar stress in vivo.
218 Immunofluorescence detected deformed nucleoli in ECs in the angiogenic retina of
219 e*Spen*$^{-/-}$ pups, accompanied by upregulated pRNA, downregulated pre-rRNA and
220 mature rRNA, and upregulated *p21* in retinal ECs (Figure 5, D–F and Supplemental
221 Figure 4G). However, we did not detect altered expression of pRNA, rRNA and *p21* in
222 adult brain ECs from e*Spen*$^{-/-}$ mice (Supplemental Figure 4H), suggesting that SPEN is
223 not required for maintaining nucleoli in quiescent ECs.

224 To determine whether pRNA upregulation is responsible for pre-rRNA
225 downregulation and p53 activation in HUVECs with SPEN knockdown, we transfected
226 HUVECs with SPENi together with a pRNA antisense oligonucleotides (ASO) to
227 knockdown pRNA (pRNAi). The result showed that pRNA knockdown completely
228 rescued the pre-rRNA expression and abrogated the SPENi-induced upregulation of
229 *p21* and *GADD45A* (Figure 5G). Consistently, a time course observation showed that
230 the pre-rRNA downregulation preceded the *p21* and *GADD45A* upregulation in
231 HUVECs with SPEN knockdown, and p53 or p21 knockdown failed to rescue SPENi-
232 induced nucleolar deformation, suggesting that SPEN knockdown activates p53 after
233 reducing pre-rRNA transcription (Supplemental Figure 4, I–K). Together, these results

234 demonstrate that SPEN knockdown upregulates pRNA to attenuate rRNA transcription,
235 leading to nucleolar stress and p53 activation in ECs.

236 To further examined the role of SPEN in ECs, we tried to upregulate SPEN in
237 HUVECs using Crispr-mediated activation of the SPEN promoter. Three sgRNAs were
238 designed, and the $SPEN^{OE3}$ (named as $SPEN^{OE}$ hereafter) exhibited highest SPEN
239 upregulation, as confirmed by RT-qPCR and immunofluorescence (Supplemental
240 Figure 5, A and B). RT-qPCR showed that the pRNA level decreased, while the pre-
241 rRNA and 5S rRNA were upregulated, but 18S and 28S rRNA did not change
242 significantly (Supplemental Figure 5, C and D). The p53 level and its downstream
243 molecules p21 and GADD45A was reduced (Supplemental Figure 5E). Cell
244 proliferation increased mildly as shown by the cell cycle analysis, accompanied by
245 enhanced sprouting ability (Supplemental Figure 5, F and G). These results further
246 indicate that SPEN represses pRNA to facilitate rRNA transcription and EC
247 proliferation.

248 **Endothelial *Spen* ablation inhibits tumor growth.** Tumor ECs exhibit higher
249 expression of ribosome-related genes (9–11). In human lung cancer biopsies,
250 immunostaining showed that lower endothelial SPEN level correlated with lower TNM
251 and AJCC stages, and higher endothelial SPEN level correlated with more lymph node
252 metastasis (Figure 6A and Supplemental Figure 6A). Moreover, low endothelial SPEN
253 level correlated with extended patient overall survival (Figure 6B). Consistently, in
254 gastric cancer and breast cancer, lower endothelial SPEN expression correlated with
255 extended patient survival (Supplemental Figure 6, B and C). In TECs from Lewis lung

256 carcinoma (LLC)-bearing mice, the *Spen* mRNA level increased along with tumor
257 progression (Supplemental Figure 6D). Therefore, high endothelial SPEN level
258 positively correlates with tumor progression in both human and mouse models.

259 Then, we inoculated SPEN deficient and control mice with LLC or B16-F10
260 melanoma cells (Supplemental Figure 2B and Supplemental Figure 6E). Tumor growth
261 was retarded in endothelial SPEN deficient mice compared with the control (Figure 6C
262 and Supplemental Figure 6, F-H). Tumor cell proliferation and tissue hypoxia were
263 attenuated in endothelial SPEN deficient mice (Figure 6, D and E). To evaluate
264 metastasis, LLC tumors were resected on 14th day post inoculation (dpi), when tumors
265 were grossly comparable between the control and SPEN deficient mice, and the mice
266 were maintained for 28 more days. Endothelial SPEN deficiency markedly reduced
267 lung metastasis, consistent with decreased circulating tumor cells (CTCs) (Figure 6, F
268 and G, and Supplemental Figure 6I). Overall survival was extended in e*Spen*$^{-/-}$ mice
269 (Figure 6H). These data demonstrate that endothelial SPEN deficiency represses tumor
270 growth and metastasis.

271 **Endothelial *Spen* ablation leads to tumor vessel normalization.** We evaluated tumor
272 vessel phenotype under endothelial SPEN deficiency. Immunostaining of CD31, α-
273 SMA, NG2, and laminin showed that tumor vessel density decreased, accompanied by
274 more regularly organized vasculature as shown by vessel reconstruction, and increased
275 pericytes and basement membrane coverage in e*Spen*$^{+/-}$ and e*Spen*$^{-/-}$ mice, suggesting
276 normalized tumor vessels (Figure 7A). A similar phenotype was observed in e*Spen*$^{-/-}$
277 mice inoculated with B16-F10 cells (Supplemental Figure 7, A–C). Cisplatin (CDDP)

278 is one of the most widely used chemotherapeutics in cancer. Tumor vessel
279 normalization is expected to enhance the efficacy of CDDP in tumor treatment (51).
280 We treated tumor-bearing mice of different genotypes with CDDP. The results showed
281 that endothelial SPEN deficiency markedly enhanced the efficacy of CDDP, as shown
282 by reduced tumor growth and increased tumor tissue necrosis (Figure 7, B and C and
283 Supplemental Figure 7D).

284 At the molecular level, SPEN deficiency increased the expression of EC junctional
285 proteins VE-cadherin and ZO-1 (Figure 8A). Functionally, endothelial *Spen* ablation
286 increased vessel perfusion and reduced leakage (Figure 8B). Consistent with in vitro
287 data, RNA-seq showed that SPEN-deficient TECs exhibited reduced expression of cell
288 cycle-related genes and angiogenesis-related genes, as confirmed by RT–qPCR and
289 immunoblotting (Figure 8, C–E and Supplemental Figure 7, E and F). These results
290 indicate that endothelial SPEN deficiency results in tumor vessel normalization.

291 **p53 deficiency abrogates *Spen* ablation-induced tumor vessel normalization.** In
292 human lung cancer biopsies, in situ hybridization of pRNA and pre-rRNA and SPEN
293 immunofluorescence in TECs showed that high SPEN level negatively correlates with
294 pRNA level, and positively correlates with pre-rRNA level (Supplemental Figure 7, G-
295 I). Then, we examined the expression of rRNA- and p53-related genes in TECs derived
296 from the e*Spen*$^{-/-}$ and control mice. KEGG analysis of differentially co-upregulated
297 genes in transcriptomic data of SPEN-deficient TECs and SPENi-transfected HUVECs
298 revealed that p53 signaling pathway was enriched in the top 20 markedly changed
299 entries, consistent with that p53 signalling is critical for *Spen* ablation-induced tumor

300 vessel normalization (Supplemental Figure 8, A–C). RT-qPCR confirmed that,
301 consistent with in vitro results, pRNA was upregulated, while pre-rRNA, 18S, 5.8S and
302 28S rRNAs, as well as *Rpl5*, *11*, and *23* mRNAs, were concomitantly downregulated,
303 in SPEN-deficient TECs (Figure 9, A–C). p53 was upregulated at protein but not mRNA
304 level, while p21 was upregulated at both mRNA and protein level in SPEN deficient
305 TECs (Figure 9, D and E). These results are in line with that endothelial SPEN
306 deficiency represses tumor angiogenesis by activating p53 via nucleolar stress induced
307 by unleashed pRNA expression.

308 To solidify the role of p53 in *Spen* ablation-induced tumor vessel normalization,
309 we crossed Cdh5-Cre^{ERT2}-SPEN^{f} mice with *p53*-floxed (*p53*^{f}) mice to obtain Cdh5-
310 Cre^{ERT2}-SPEN$^{f/f}$ mice on the endothelial *p53*$^{+/f}$ (e*p53*$^{+/-}$) background. Tamoxifen-
311 induced wild-type (Ctrl), e*Spen*$^{-/-}$, e*p53*$^{+/-}$, and e*Spen*$^{-/-}$e*p53*$^{+/-}$ mice were inoculated
312 with LLC cells. Heterozygous endothelial p53 disruption (e*p53*$^{+/-}$) almost completely
313 abrogated SPEN disruption (e*Spen*$^{-/-}$)-induced tumor repression (Figure 9F and
314 Supplemental Figure 8, D and E). Immunostaining showed that while *Spen* ablation
315 resulted in decreased hypoxia accompanied by decreased vessel density and increased
316 pericyte coverage, these phenotypes were reversed by p53 haploinsufficiency (Figure
317 9, G–J). The p53 haploinsufficiency also cancelled *Spen* ablation-induced improvement
318 of vessel function as determined by the vessel perfusion and leakage assays (Figure 9,
319 G, K and L). These results demonstrate that SPEN deficiency normalizes tumor vessels
320 by activating p53.

321 SPEN is a repressor of Notch signalling, which plays a pivotal role in vessel
322 development (22, 52). However, Notch downstream genes Hairy/enhancer-of-split
323 related with YRPW motif protein 1 (*HEY1*) and Hairy and enhancer of split 1 (*HES1*)
324 were not upregulated in HUVECs or TECs with SPEN knockdown or ablation,
325 respectively (Supplemental Figure 8, F and G), suggesting that SPEN does not repress
326 but rather is required for the canonical Notch signalling in ECs. Double knockout of
327 *Spen* and recombination signal binding protein for immunoglobulin kappa J region
328 (*Rbpj*) (53), the transcription factor mediating Notch signalling, did not rescue the *Spen*
329 ablation phenotype (Supplemental Figure 8, H and I), suggesting that SPEN deficiency
330 does not normalize tumor vessels by activating Notch.

331 **The RNPI inhibitor CX-5461 normalizes tumor vessels and improves**
332 **chemotherapy.** Our data have suggested that induction of nucleolar stress by SPEN
333 deficiency-induced pRNA upregulation could normalize tumor vessels and therefore
334 serves as a target for AAT. To solidify this finding, we synthesized pRNA ASOs and
335 verified the effect on ECs in vitro (Supplemental Figure 9A). We set up LLC tumors in
336 e*Spen*$^{-/-}$ and control mice, and injected the pRNA ASO intra-tumorally from 10 dpi.
337 The result showed that, while pRNA ASO slightly promoted tumor growth in the
338 control, it abrogated endothelial SPEN deficiency-induced tumor suppression
339 (Supplemental Figure 9B). Moreover, pRNA ASO partially but substantially reversed
340 SPEN deficiency-induced tumor vessel normalization, as shown by increased vessel
341 density and decreased pericyte coverage (Supplemental Figure 9C). Furthermore, we
342 constructed liposome nanoparticles (LNP) conjugated with cyclo (Arg-Gly-Asp-D-

343 Tyr-Lys) peptide (c(RGDyK)), which targets αvβ3 integrin receptors with high affinity
344 on TECs (54, 55). The LNP was loaded with a plasmid expressing pRNA (LNP-pRNA),
345 which could be taken by TECs and increased pRNA level in TECs after infusion (Figure
346 10A and Supplemental Figure 9, D and E). Infusion of LNP-pRNA or LNP-Ctrl into
347 tumor-bearing mice showed that LNP-pRNA mildly repressed tumor growth, and
348 tumor vessel density decreased while pericyte coverage and vessel perfusion were
349 improved in LNP-pRNA-treated mice (Figure 10, B–D and Supplemental Figure 9, F–
350 H). These results suggest that upregulating pRNA could normalize tumor vessels while
351 downregulating pRNA has the opposite effect.

352 Because rRNA gene transcription is driven by RNPI, we assessed whether CX-
353 5461, an RNPI inhibitor under clinical trial, could induce tumor vessel normalization
354 (27–30). Treating HUVECs with CX-5461 downregulated pre-rRNA and upregulated
355 *p21* dose-dependently, with an enlarged cell size resembling that observed under SPEN
356 knockdown (Supplemental Figure 10, A and B). CX-5461 suppresses tumor growth in
357 mice (27). To exclude the proliferation inhibition of CX-5461 on tumor cells, which
358 may influence tumor vessels, we tried different dosing schedules and found that when
359 mice bearing LLC tumors were orally administered with 50 mg/kg CX-5461 every two
360 days from 7 to 14 dpi, tumor growth did not change significantly (Supplemental Figure
361 10C). Upon this dosing schedule, tumor tissues showed a normalized vasculature, as
362 manifested by a reduced vessel density, increased pericyte and basement membrane
363 coverage, and improved tumor vasculature as shown by vessel reconstruction, and
364 increased expression of EC junctional proteins VE-cadherin and ZO-1 (Figure 10, E

365 and F). Moreover, CX-5461 treatment increased vessel perfusion and attenuated
366 leakage (Figure 10G). When CX-5461 and CDDP were applied in combination, CX-
367 5461 enhanced the efficacy of CDDP (Figure 10H and Supplemental Figure 10D). We
368 monitored spleen T and B lymphocytes, which are expect to undergo significant
369 proliferation and likely require enhanced ribosome biogenesis, in mice treated with CX-
370 5461 at the dosage generating the size-matched tumors. The results showed that T and
371 B lymphocytes in spleen were not significantly influenced by CX-5461 in our
372 experiments, although spleen size decreased slightly (Supplemental Figure 10, E–H).
373 These results demonstrate that RNPI inhibition with inhibitors such as CX-5461
374 induces tumor vessel normalization, and improves chemotherapy.

375 **Discussion**

376 The tumor vasculature has been a therapeutic target of cancer for decades due to its
377 characteristic abnormal structure and hyperactive TECs. AAT normalizes tumor
378 vasculature, leading to attenuated hypoxia and vessel leakage, improved vessel
379 perfusion, and reduced metastasis, and thereby mitigating tumor malignancy (2, 3).
380 However, because tumors by principle employ physiological mechanisms for
381 angiogenesis, discovering efficient targets for AAT has been a long-term challenge (3,
382 4, 6). In this study, we have revealed for the first time that ribosome biogenesis is a
383 AAT target (Supplemental Figure 10I). Tumor growth stimulates active angiogenesis,
384 which requires the RNPI-mediated transcription of rRNA genes and active ribosome
385 biogenesis in TECs (9–11). Activated TECs upregulate their SPEN to facilitate rRNA
386 gene transcription by repressing pRNA, and SPEN is therefore required for tumor

387 angiogenesis. In the absence of SPEN, pRNA is upregulated and rRNA gene
388 transcription is repressed, thereby disrupting ribosomal biogenesis. This triggers the
389 p53-mediated nucleolar stress response, which results in reduced EC proliferation and
390 tumor vessel normalization. Forced pRNA expression or RNPI inhibitors (CX-5461)
391 can mimic the effect of SPEN deficiency in tumor vessels, leading to tumor vessel
392 normalization, which has been shown previously (27–30, 56). It is noteworthy that
393 SPEN haploinsufficiency results in similar but less severe phenotype as complete *Spen*
394 ablation, suggesting that the effect of ribosome biogenesis inhibition on tumor
395 angiogenesis is dose-dependent. Together, our results demonstrate that ribosome
396 biogenesis is a druggable target for AAT of tumors.

397 AAT targeting RNPI could have several advantages. Firstly, *p53* is highly mutated
398 in cancer cells but largely intact in tumor microenvironment cells including TECs.
399 Therefore, RNPI-targeted AAT could be expected to be effective irrespective of *p53*
400 mutation. p53 has been shown to limit angiogenesis by interfering with the central
401 regulators of hypoxia that mediate angiogenesis and by inhibiting proangiogenic factor
402 production and increasing endogenous angiogenesis inhibitor production (57).
403 Although p53 mediates endothelial senescence and induces endothelial dysfunction
404 under different conditions, its activation has been shown to exert an antiangiogenic
405 effect on tumors (58–61). Secondly, nucleolar stress induced by SPEN knockdown does
406 not increase the apoptosis of ECs. This is in contrast to AATs disrupting VEGF
407 signalling, which is required for EC survival (1). Increased TEC death can lead to
408 aggravated hypoxia and tumor metastasis (62). The mechanism of EC survival under

409 nucleolar stress could be related with increased autophagy, but further investigations
410 are needed to address this question (63). In addition, we noticed that cell size increases
411 under SPEN deficiency or RNPI inhibition, which could be related with disturbed
412 ribosome biogenesis (64). Lastly, our data showed that the combination of CX-5461
413 and CDDP markedly enhanced the efficacy of CDDP in mice, supporting the use of
414 RNPI inhibitors in combination with other strategies as a treatment for solid tumors.
415 However, considering potential off-target effects of RNPI inhibitors and the complex
416 mechanisms controlling ribosome biogenesis (65), detailed studies are required to
417 define the dosage and time window required for RNPI inhibitors to serve as an efficient
418 adjuvant of other anti-tumor therapies such as chemotherapy and immunotherapy.

419 Nucleoli are specialized, membrane-lacking nuclear structures formed by phase
420 separation (66). The major functions of nucleoli include transcribing and processing
421 rRNA and assembling ribosomes (14, 15). To fulfil these tasks, nucleoli are organized
422 into layered structures, and each structural layer accommodates specific biochemical
423 reactions (38, 66). Numerous extrinsic and intrinsic insults disrupt the function and
424 elegant structure of nucleoli, leading to p53-mediated nucleolar stress (16–18). Our data
425 demonstrated that SPEN deficiency resulted in nucleolar stress in ECs, as manifested
426 by the disordered nucleolar structure, reduced RP expression, and p53 activation, which
427 was responsible for endothelial growth arrest and tumor vessel normalization in this
428 study. SPEN possesses several RNA recognition domains (RRMs) and functions as an
429 RNA-binding protein (20, 23, 24). Protein structure prediction suggests that SPEN
430 contains large stretches of intrinsic disordered regions (IDRs). These two properties are

431 shared by many proteins participating in phase separation (38). However, our
432 immunostaining of HUVECs with SPEN antibodies showed that SPEN localized
433 outside nucleoli. This suggests that SPEN regulates nucleolar function, rather than
434 constitutes their structure. Indeed, we demonstrate that SPEN deficiency reduces rRNA
435 transcription by upregulating pRNA, a lncRNA derived from the spacer promoter, and
436 inhibits the activity of the gene promoter of rDNA repeats. pRNA knockdown with an
437 ASO not only rescues pre-rRNA expression but also compromised p53 activation,
438 suggesting that SPEN normally represses pRNA to maintain rRNA gene expression.
439 This could physiologically balance the active and inactive rDNA repeats in the rDNA
440 array, which is a suggested function of pRNA (46). The reduced rRNA synthesis
441 induced by SPEN deficiency disrupts the assembly of newborn ribosomes, leading to
442 the redirection of RP and the activation of p53 via MDM2 (16–18). However, pRNA
443 transcription is dependent on RNPI but not RNPII (46), and the mechanism by which
444 SPEN represses the RNPI-mediated transcription of spacer promoters in rDNA repeats
445 has not been elucidated. Moreover, p53 expression is under the control of numerous
446 mechanisms, and other mechanisms underlying p53 upregulation could be involved,
447 and worth to investigate further in future.

448 SPEN is a large protein containing several functional domains including N-
449 terminal RRMs, a C-terminal SPOC domain, and motifs interacting with transcription
450 factors located between the N- and C-terminals (19, 20, 24). SPEN does not possess
451 DNA-binding domains, so that SPEN fulfils its transcription repressor functions by
452 interaction with recruiting molecules such as lncRNAs or DNA-binding proteins. At

453 spacer promoter regions in which pRNA transcription starts, the factors responsible for
454 SPEN recruitment have not been defined. One possibility is CTCF, which binds rDNA
455 repeats near the spacer promoter and transcription termination site. CTCF influences
456 the topological architecture of rDNA by forming the chromatin conformation required
457 for RNPI recruitment and rDNA transcription. The lncRNA SRA binds to and regulates
458 the function of CTCF (25). SRA also binds SPEN (20). It is therefore possible that
459 SPEN binds CTCF via SRA and influences the conformation of rDNA. Moreover, a
460 recent report showed that SPEN binds directly to endogenous retroviral (ERV) RNAs
461 and participates in ERV silencing (26). Some rDNA repeats are silenced by epigenetic
462 mechanisms, while others remain active (14, 15). Whether SPEN participates in
463 silencing rDNA repeats in a manner similar to that of ERV is worthy of further
464 investigation. Moreover, the SPOC domain provides a protein-interacting platform to
465 recruit transcription repressors such as HDACs, EZH2, NcoR and m6A modification
466 enzymes (24). It will be interesting to examine the roles of these enzymes in SPEN-
467 mediated nucleolar homeostasis.

468 It has been demonstrated that SPEN is recruited by interacting with RBPJ to
469 thereby repress canonical Notch signalling (22). However, SPEN could also be
470 recruited to chromatin to promote heterochromatin formation and modify gene
471 expression networks at the epigenetic level (24, 26). In ECs, our data showed that the
472 Notch downstream genes *HES1* and *HEY1* were not upregulated under SPEN deficiency,
473 suggesting that SPEN does not repress but is rather required for the canonical Notch
474 signalling in ECs. This is consistent with previous findings in *Drosophila* (67, 68).

475 Functionally, although both of the SPEN deficiency and the RBPJ deficiency inhibit
476 tumor growth, SPEN deficiency normalizes while RBPJ deficiency disrupts tumor
477 vasculature, and disruption of both leads to normalized tumor vessels. Therefore, more
478 studies are required for elucidating the relationship between SPEN and Notch in ECs.

479 **Methods**

480 **Human samples.** Human lung adenocarcinoma tissue microarrays (HLugA180Su07,
481 HLugA180Su08), human gastric cancer tissue microarray (HStmA180Su30) and
482 human breast cancer tissue microarray (HBreD136Su02) were provided by Shanghai
483 Outdo Biotech Co., Ltd. (Shanghai, China) (Supplemental Table 1–4).

484 **Animals.** Mice were maintained in a specific pathogen-free (SPF) facility. *Spen*-floxed,
485 *Cdh5-Cre*^{ERT2} transgenic, and *Rbpj*-floxed mice were described previously (31, 53, 69).
486 *p53*-floxed mice were purchased from Shanghai Model Organisms Center, Inc.
487 (Shanghai, China). Mice were backcrossed with C57BL/6J mice for more than 6
488 generations, and genotyped by PCR using tail DNA as a template. To induce Cre-
489 mediated recombination, 6–8-week-old male or female mice were injected i.p with 100
490 μl of tamoxifen (20 mg/ml, Sigma, T5648), while P1 pups were injected subcutaneously
491 (s.c) with 2.5 μl of tamoxifen (Supplemental Figure 2B).

492 For mouse tumor models, LLC (5×10^6) or B16-F10 (1×10^6) cells were inoculated
493 s.c in the right back of trunks one day after the last tamoxifen injection and maintained
494 for 21 or 16 days post inoculation (dpi), respectively. Tumor size was monitored using
495 a caliper and calculated as $\pi \times [d^2 \times D]/6$ (d, short diameter, D, long diameter). In some
496 experiments, CDDP (2.5 mg/kg, Selleck, S1166) was injected i.p every three days from

497 7 dpi. CX-5461 (50 mg/kg, Selleck, S2684) was administered by gastric gavage every
498 two days from 7 dpi. LNP (25 μg DNA, 200 μL/mouse, see below) was injected i.v
499 every three days from 7 dpi. The 2′-O-(2-Methoxyethyl) phosphorothioate ASO to
500 mouse pRNA (Shanghai Integrated Biotech Solutions Co., Ltd, Shanghai, China) was
501 injected intra-tumorally at a dosage of 5 nmol per mouse every three days from 10 dpi.
502 Three ASO were tested (5'-GGACCTCAAAGGAACAACTG, 5'-
503 CGGAGAACTGATAAGACCGA, and 5'-GGTCCAATAGGAACAGATAG), with
504 the first one employed in further study. To evaluate metastasis, LLC cells were
505 transduced with luciferase (luciferase-LLC) or GFP (GFP-LLC) lentivirus (GeneChem,
506 Shanghai, China). Tumors of luciferase-LLC were surgically removed on 14 dpi after
507 anaesthetization with 1% pentobarbital sodium. On day 28 after tumor resection, mice
508 were injected with D-luciferin (150 mg/kg, Yeasen, Shanghai, China, 40902ES01) and
509 sacrificed 8 min later. Their lungs were removed, photographed, and analysed with a
510 bioluminescence imaging system (IVIS Lumina II, Perkin-Elmer), followed by
511 histological staining. To detect CTCs, the GFP-LLC cells were inoculated, and blood
512 was collected on 21 dpi. After erythrolysis with red lysis buffer (Cwbio, Beijing, China,
513 CW0613), GFP^+ cells were counted under a fluorescence microscope (NI-E, Nikon).
514 For survival analysis, LLC tumors were surgically removed on 21 dpi, and the survival
515 of mice was plotted by the Kaplan–Meier method.

516 A Matrigel plug assay was performed by injecting 0.3 ml of Matrigel (Corning,
517 354230) containing 400 ng/ml VEGF (SinoBio, Beijing, China, 50159-MNAB) and
518 250 ng/ml bFGF (SinoBio, 50037-M07E) into the mouse groin. The plugs were

519 recovered on day 7 and fixed in 4% paraformaldehyde (PFA) overnight. Masson
520 trichrome staining was conducted using a kit (Servicebio, Wuhan, China, G1006).
521 **Histology.** Tissues were fixed in 4% PFA at 4 °C overnight and embedded in paraffin
522 routinely. Samples were cut into 4-μm-thick sections and then subjected to
523 haematoxylin and eosin (H&E) staining. Fluorescence triple staining was conducted
524 using a TSAPLus Fluorescence Triple Staining Kit (Servicebio, G1236).
525 For immunofluorescence, tissues were fixed in 4% PFA at 4 °C for 4 h, followed
526 by dehydration in 30% sucrose-PBS overnight. The samples were then embedded in
527 optimal cutting temperature (OCT) compound (Sakura, 4583). Frozen blocks were
528 sectioned at 10 μm or 60 μm thickness, dried at room temperature for 2 h, and blocked
529 with PBS containing 5% BSA and 0.3% Triton X-100 for 1 h at room temperature. The
530 samples were incubated overnight at 4 °C with primary antibodies. After washing, the
531 sections were incubated with secondary antibodies at room temperature for 2 h and
532 counterstained with Hoechst (Sigma, 94403) for 15 min at room temperature. Cell
533 samples on coverslips were fixed with 4% PFA for 30 min and blocked with PBS
534 containing 5% BSA and 0.3% Triton X-100 for 30 min at room temperature. For whole-
535 mount retinal staining, eyeballs were harvested and fixed in 4% PFA at 4 ℃ for 2 h,
536 and the retinas were dissected and stained as described above. EdU labelling was
537 performed by injecting i.p EdU (50 μg/g, RiboBio, Guangzhou, China, C00053) 4 h
538 before euthanasia, and stained using a commercial Cell Light EdU Apollo® 567 In Vitro
539 Kit (RiboBio, C10310-1). RNA-ISH combined with fluorescent IHC was conducted
540 using RNA-Protein Co-Detection Ancillary Kit (323180; ACD Bio) according to the

541 provided protocol. The human pre-rRNA and pRNA (+551 ~ +2922 and -415 ~ -32,
542 respectively, Genebank accession # U13369.1) probes were ordered from ACD Bio.
543 Images were captured under a fluorescence microscope (NI-E, Nikon), confocal
544 microscope (A1R, Nikon), or SIM microscope (N-SIM S, Nikon). The
545 immunofluorescence staining pictures of human biopsies were quantified by
546 TissueFAXS Q+ 2D/3D panoramic tissue cell imaging quantitative analysis system.
547 The expression of SPEN, pre-rRNA and pRNA in $CD31^+$ ECs were quantified using
548 IMARIS 9.0.1. Antibodies are listed in Supplemental Table 5.

549 To detect hypoxia, mice were injected i.p with pimonidazole hydrochloride (60
550 mg/kg, Cayman, 89130) 1 h prior to tumor harvesting. Cryosections were stained with
551 a Hypoxyprobe-1-Mab1 kit (Hypoxyprobe, PAb2627AP). To examine vascular
552 perfusion and leakage, mice were injected i.v with 5 mg of FITC-conjugated dextran-
553 2MD (Sigma, FD2000s) or 0.25 mg of Texas Red-conjugated dextran-70KD
554 (Invitrogen, D1864) and perfused by intracardiac infusion with PBS 15 min after the
555 injection under anaesthetization. Immunostaining was conducted as described above.

556 For transmission electron microscopy (TEM), cells were trypsinized and fixed first
557 in 2.5% glutaraldehyde and then in ferrocyanide-reduced osmium tetroxide. After
558 uranyl staining *en bloc*, samples were embedded in epoxy resin according to standard
559 procedures. Ultrathin sections were obtained and observed under an electron
560 microscope (Tecnai Spirit of FEI or JEM-1230, Japan Electronics Co., Ltd.).

561 **Cell culture and transfection.** LLC, B16-F10, and HEK-293T cells were obtained
562 from American Type Culture Collection (ATCC) and authenticated by both

563 morphological analysis and short tandem repeat profiling. Cells were maintained in
564 Dulbecco's modified Eagle's medium (DMEM) supplemented with 10% fetal calf
565 serum (FCS). HUVECs were cultured in EC medium (ScienCell, 1001) supplemented
566 with 5% fetal bovine serum (FBS), 1% EC growth supplements (ECGS) and 1%
567 streptomycin–penicillin. HUVECs were used between passages 2 and 6. CX-5461 was
568 applied at different concentrations, with 50 mM NaH_2PO_4 as the vehicle.
569 Cycloheximide (CHX) was used at the final concentration of 20 μM.

570 To isolate primary ECs, normal or tumor tissues were minced mechanically and
571 digested in 1 mg/ml collagenase I (Sigma, C0130) and 100 μg/ml DNase I (Roche,
572 10104159001) for 30 min at 37 °C. After passing through a 70-μm tissue strainer, cell
573 suspensions were centrifuged for 4 min at 1200 rpm at 4 °C, followed by erythrolysis.
574 The cells were resuspended in 90 μl of PBS containing 0.5% BSA and 2 mM EDTA
575 and mixed with 10 μl of anti-CD31-coated magnetic beads (Miltenyi, 130-097-418).
576 After incubation at 4 °C for 30 min, the cells were collected using a magnetic bead
577 collector (Miltenyi) and then washed three times with PBS containing 0.5% BSA and
578 2 mM EDTA. ECs were evaluated by flow cytometry after staining with anti-
579 endomucin.

580 Transfection of ECs with shRNA for *SPEN* (shRNA1 5'-
581 CCAGTACGCTCTACAGATA and shRNA2 5'-CCCGATCACGCCGCAAGCGAA),
582 *p53* (5'-CGGCGCACAGAGGAAGAGAAT), *p21* (5'-
583 AAGACCATGTGGACCTGTCAC), or the nonsense control (NC) was achieved by
584 lentiviral transduction at the multiplicity of infection (MOI) of 10. Transduction was

585 performed on Day 0, and the culture medium was replaced with fresh medium 24 h
586 later. Overexpression was achieved by adenovirus transduction at the MOI of 200, and
587 the culture medium was replaced with fresh medium 4 h later. Lentivirus or adenovirus
588 construction and packaging were conducted by GeneChem and Vigene Biosciences
589 (Jinan, China). The ASO of human pRNA (5'-GGACACCTGTCCCCAAAAAC) was
590 transfected with HiPerFect Transfection Reagent (Qiagen, 301705) at a final
591 concentration of 100 nM.

592 Endogenous *SPEN* gene was activated using the lentivirus CRISPR-Cas9
593 Synergistic Activation Mediator (SAM) system (Genechem Co., Ltd, Shanghai, China)
594 following the supplier's protocol (70). Briefly, HUVECs were infected with
595 lentiviruses encoding dCas9-VP64 (lenti-dCAS9-VP64-Puro) and sgRNAs (lenti-
596 sgRNA-MS2-P65-HSF1-Neo) simultaneously at the MOI of 5, and the culture medium
597 was replaced with fresh medium 24 h later. Activation of *SPEN* expression was
598 determined on day 4. Cells infected with dCas9-VP64 and non-targeting sgRNA
599 lentiviruses were used as controls. Three sgRNAs (5'-
600 TAGTCCCTCACTTCGTCGCC, 5'- GCTAGTGGAGTCCCGCTGCT, and 5'-
601 ACGAAGTGAGGGACTACAGG) were tested, and the third one ($SPEN^{OE3}$) was used
602 for further study.

603 For reporter assay, HEK-293T cells in 48-well plates (5×10^3 cells/well) were
604 transduced with SPENi lentivirus. The cells were then transfected with 200 ng of the
605 p53 reporter plasmid (p53-luc, Yeasen, 11540ES03) and 10 ng of pRL-TK (Promega,
606 E2241). The cells were harvested 24 h after transfection, and the luciferase activity was

607 analysed with the Dual-Luiferase Reporter Assay System (Promega).

608 **Time-lapse imaging.** Cells were sparsely seeded in a quartered confocal dish well or
609 6-well plate. Time-lapse images were recorded using a live cell imaging workstation
610 under a confocal microscope at 3-min intervals or a fluorescence microscope at 5-min
611 intervals. The velocity of movement was determined by Fiji v2.0.0 with the Trackmate
612 plugin.

613 **Cell proliferation and migration.** HUVECs were cultured in fresh ECM containing
614 1% FBS for 24 h and then in ECM with 5% FBS for an additional 24 h. The cells were
615 then cultured in medium containing 50 μM EdU (RiboBio, Guangzhou, China, C10310-
616 1) for 2 h, fixed with 4% PFA at room temperature for 30 min, and stained with Cell
617 Light EdU Apollo® 567 In Vitro Kit (RiboBio, C10310-1). Images were captured under
618 a fluorescence microscope.

619 For migration, cells were seeded in 24-well plates at 1×10^5 cells/well and allowed
620 to reach confluence over the next 24 h. A scratch was made using a pipette tip, and the
621 closure of the scratch was monitored for 12 h in ECM containing 1% FBS.

622 **Fibrin bead sprouting assay.** HUVECs expressing EGFP were cultured in fresh EGM-
623 2 medium (Lonza, CC-3162). HUVECs were incubated with Cytodex 3 microbeads
624 (400 cells per bead, Sigma, C3275) at 37 °C for 4 h and then transferred into 12-well
625 plates containing EGM-2 medium and cultured overnight. The next day, microbeads
626 were embedded in fibrinogen (Sigma, F4883) containing 0.625 U/ml thrombin (Sigma,
627 T4648) and 0.15 U/ml aprotinin (Sigma, A1163) at a density of 100 beads/ml in a 48-
628 well plate, and 0.5 ml EGM-2 medium was added to mouse lung fibroblasts (MRC5)

629 (1 × 10^4 cells/well). The cells were cultured for 4 days with two medium changes.
630 Images were captured under a fluorescence microscope, and sprouting was quantified
631 by counting the number or length of sprouts.

632 **RT–qPCR.** Total RNA was extracted using the TRIzol reagent (Invitrogen, 15596018).
633 cDNA was synthesized with a reverse transcription kit (Takara, RR036A). Real-time
634 PCR was conducted using a SYBR Premix Ex Taq Kit (Takara, RR820A) on an ABI
635 QuantStudio 5 real-time PCR system (Thermo Scientific), with β-actin as an internal
636 control. For strand-specific RT–qPCR, RNA was extracted with the RNAprep Pure Kit
637 (Tiangen, Beijing, China, DP430), and genomic DNA was removed with RNase-free
638 DNase I. Strand-specific (ss) primers were used to synthesize sense or antisense chains
639 using the Transcriptor First Strand cDNA Synthesis Kit (Roche, 4897030001), followed
640 by real-time PCR. The 7SK sense transcript was used as a control. Primers are listed in
641 Supplemental Table 6.

642 **ChIP-qPCR assay.** ChIP was performed using a SimpleChIP Enzymatic Chromatin IP
643 Kit (Cell Signalling Technology, 9003). Briefly, HUVECs were treated with 1%
644 formaldehyde. Crosslinked chromatin was digested with micrococcal nuclease for 20
645 min at 37 °C and sonicated. Antibodies or control immunoglobulin G (IgG) was applied
646 to pull down fragmented chromatin, and chromatin-antibody complexes were collected
647 with Protein-G beads and washed extensively. After elution, DNA-protein crosslinks
648 were reversed by incubation at 65 °C for 2 h. Precipitated DNA fragments were
649 extracted and analysed by qPCR, and the results were normalized to those of the
650 genomic DNA preparations. Primers are listed in Supplemental Table 6.

651 **Fluorescence-activated cell sorter (FACS).** Cells were collected routinely. After
652 erythrolysis, cells were resuspended in PBS containing 2% inactivated FBS and 0.01%
653 NaN_3 and stained in dark for 30 min with antibody cocktails on ice. Analysis was
654 performed on a FACS CantoII™ instrument (BD Pharmingen). Cell viability was
655 evaluated with 7-amino-actinomycin D (BD Pharmingen, 559925). Data were analysed
656 using FlowJo V.10 software (TreeStar). Antibodies are listed in Supplemental Table 5.
657 For cell cycle analysis, HUVECs were trypsinized and fixed in 70% ethanol
658 overnight. The fixed cells were incubated in PBS containing 0.2% Triton X-100, 100
659 μg/ml RNase A (Roche, 10109142001), and 50 μg/ml propidium iodide for 30 min at
660 37 °C and analysed with a FACS Calibur™ flow cytometer (BD Biosciences) or
661 CytoFLEX flow cytometer (Beckman Coulter).
662 **Preparation of cationic lipid nanoparticles (LNP).** To prepare LNP (Xi'an Ruixi
663 Biological Technology Co., Ltd, Xian, China) (54, 55), 60 mg soybean lecithin (SPC),
664 6 mg N-[1-(2,3-dioleoyloxy)-propyl]-N,N,N-trimethylammonium methyl-sulfate
665 (DOTAP), 1.2 mg 1.2-distearoyl-sn-glycero-3-phosphoethanolamine-N-[methoxy
666 (polyethylene glycol)-2000] (DSPE-PEG2000), 2.4 mg 1,2-distearoyl-sn-glycero-3-
667 phosphoethanolamine-N-[methoxy(polyethylene glycol)-2000]-c(RGDyK) (DSPE-
668 PEG2000-cRGD) and 3.6 mg cholesterol were dissolved in 2 ml ethanol and transferred
669 to solanum-shaped flask. Plasmids (pcDNA3.1, pcDNA3.1-pRNA [-232 ~ -1 of mouse
670 rDNA, genebank accession # BK000964.3] (71, 72), or pIRES2-dsRED) DNA (3 mg)
671 were dissolved in 50 mM citrate buffer (pH4.0) containing 25% ethanol, and then
672 slowly added into the flask. After 20 min of incubation, the mixture was treated with

673 ultrasound and liposome extruder (100 nm filter). Free DNA was removed by a
674 nanodialysis device. The encapsulation efficiency was between 86% and 91%.
675 **RNA-seq.** Total RNA was extracted using the TRIzol reagent from HUVECs or
676 primary TECs. RNA quality was evaluated using an Agilent 2200 Tape Station (Agilent
677 Technologies) and RNase-free agarose gel electrophoresis. mRNA was enriched with
678 oligo(dT) beads, fragmented with fragmentation buffer, and reverse transcribed with
679 random primers. Second-strand cDNA was synthesized, and the cDNA fragments were
680 purified with a QiaQuick PCR extraction kit (Qiagen), end repaired, and ligated to
681 Illumina sequencing adapters. The ligation products were size-selected by agarose gel
682 electrophoresis, amplified, and sequenced on an Illumina NovaSeq6000 platform for
683 HUVECs (Gene Denovo Biotechnology Corporation, Guangzhou, China) and on an
684 Illumina Xten platform for TECs (Annoroad, Beijing, China). The principal component
685 analysis (PCA) was performed based on the fast.prcomp function of gmodels in R
686 package (version 3.6.0), where the parameter is set to scale = f, center = t. After
687 dimensionality reduction, the PCs were ranked based on the percentage of variance by
688 each PC and the first two PCs were extracted to draw a scatter plot with the geom_point
689 function in ggplot2 package (version 2_3.3.5). Other bioinformatic analyses, including
690 the differential gene expression analysis, pathway analysis, and gene set enrichment
691 analysis (GSEA), were performed using the OmicShare tools (73), a free online
692 platform for data analysis, TB Tools software and GSEA2.2.4.
693 **Immunoblotting.** Cell lysates were prepared with RIPA buffer (Beyotime, Shanghai,
694 China, P0013B) containing 10 mM phenylmethanesulfonyl fluoride (PMSF, Thermo

695 Scientific, 36978). Proteins were separated by sodium dodecyl sulfate-polyacrylamide
696 gel electrophoresis (SDS–PAGE) and blotted onto polyvinylidene fluoride (PVDF)
697 membranes. The membranes were blocked with 5% skim milk in PBS-0.1% Tween 20
698 and then incubated with primary antibodies at 4 °C overnight, followed by washing and
699 incubation with secondary antibodies at room temperature for 2 h. After washing, the
700 blots were developed with enhanced chemiluminescence (Thermo Scientific) and
701 detected using a ChemiScope Imaging System (Clinx Science Instruments, Shanghai,
702 China). β-actin was used as an internal reference. A Nuclear and Cytoplasmic Protein
703 Extraction Kit (Beyotime, P0028) was used to separate nuclear and cytoplasmic
704 proteins, with β-actin and lamin A/C serving as references for cytoplasmic and nuclear
705 proteins, respectively.

706 **Immunoprecipitation.** Cell lysates were prepared and quantified. Primary antibodies
707 (10 μg) or isotype control was incubated with 30 μl of Protein-G magnetic beads
708 (Invitrogen, 10004D) for 2 h at 4 °C with gentle rotation. Then, the antibody-coated
709 beads were mixed with cell lysates with equal amounts of total proteins and incubated
710 at 4 °C overnight. The beads were washed three times with ice-cold PBS and boiled for
711 15 min in reductive loading buffer before SDS–PAGE and immunoblotting. For the
712 detection of MDM2/RPL5/RPL11/5S rRNA complex, cell lysates were first subjected
713 to ultracentrifugation at 20,0000 × g for 2 h, 4 °C, followed by immunoprecipitation
714 and detection routinely (74).

715 **Statistics.** Quantitative analysis was performed using Image-Pro Plus 6.0, Fiji v2.0.0,
716 IMARIS 9.0.1, FlowJo 7.6.1 and FlowJo V.10 software. Statistical analysis was

717 performed using GraphPad Prism 8.0 software. All quantitative data are presented as
718 the means ± SEMs. Statistical significance was calculated using the unpaired two-sided
719 t-test (for two groups) or one-way ANOVA with Tukey's multiple comparison test (for
720 more than two groups). Chi-square χ^2 analyses were performed to compare the
721 distributions of tumor stages among the human lung adenocarcinoma tissue cohort.
722 Log-rank (Mantel–Cox) tests were employed for survival analysis. Correlation between
723 SPEN and RNA expression in human lung adenocarcinoma tissue cohort was
724 determined by Spearman's rank-order correlation analysis. $P < 0.05$ was considered
725 statistically significant.

726 **Study approval.** Protocols involving human samples were approved by the Ethics
727 Committee of Xijing Hospital, Fourth Military Medical University. The animal
728 experiments were approved by the Animal Experiment Administration Committee of
729 Fourth Military Medical University.

730 **Data availability.** Original data of RNA-seq are available in the Genome Sequence
731 Archive GSA) database (https://bigd.big.ac.cn/gsa) with accession #s: HRA000788 for
732 HUVECs and CRA004085 for TECs. See complete unedited blots in the supplemental
733 material. Values for all data points in graphs are reported in the supporting data values
734 file.

735 **Acknowledgements**

736 This study was supported by the National Natural Science Foundation (31730041,
737 31671523, 82003110, 81900870) of China and the Key Research and Development
738 Program of Shaanxi Province (2023-YBSF-118).

Author contributions

YZY, YXC, and ZJYL performed experiments and collected data. LL assisted with experiments and data collection. GCC, ZPR, RB, and DJL helped in cell and molecular biology experiments. LY, SJX, WRN, FXX, CB and XT assisted with animal maintenance and experiments. HH designed the experiments and prepared the manuscript. YZY, YXC, and ZJYL share first authorship, and the order in which they are listed was determined by workload.

Conflict of interest

The authors have declared that no conflict of interest exists.

749 **References**

750 1. Carmeliet P, and Jain RK. Molecular mechanisms and clinical applications of
751 angiogenesis. *Nature.* 2011;473(7347):298–307.
752 2. Lugano R, et al. Tumor angiogenesis: causes, consequences, challenges and
753 opportunities. *Cell Mol Life Sci.* 2020;77(9):1745–70.
754 3. Martin JD, et al. Normalizing function of tumor vessels: progress, opportunities,
755 and challenges. *Annu Rev Physiol.* 2019;81:505–34.
756 4. Jászai J, and Schmidt MHH. Trends and challenges in tumor anti-angiogenic
757 therapies. *Cells.* 2019;8(9).
758 5. Cao Y, et al. Forty-year journey of angiogenesis translational research. *Sci*
759 *Transl Med.* 2011;3(114):114rv3.
760 6. Li X, et al. Hallmarks of endothelial cell metabolism in health and disease. *Cell*
761 *Metab.* 2019;30(3):414–33.
762 7. Itatani Y, et al. Resistance to anti-angiogenic therapy in cancer-alterations to
763 anti-VEGF pathway. *Int J Mol Sci.* 2018;19(4):1232.
764 8. Haibe Y, et al. Resistance mechanisms to anti-angiogenic therapies in cancer.
765 *Front Oncol.* 2020;10:221.
766 9. Goveia J, et al. An integrated gene expression landscape profiling approach to
767 identify lung tumor endothelial cell heterogeneity and angiogenic candidates.
768 *Cancer Cell.* 2020;37(1):21–36.e13.
769 10. Zhao Q, et al. Heterogeneity and chimerism of endothelial cells revealed by
770 single-cell transcriptome in orthotopic liver tumors. *Angiogenesis.*

771 2020;23(4):581–97.

772 11. Rohlenova K, et al. Single-cell RNA sequencing maps endothelial metabolic
773 plasticity in pathological angiogenesis. *Cell Metab.* 2020;31(4):862–77.e14.

774 12. Pelletier J, et al. Ribosome biogenesis in cancer: new players and therapeutic
775 avenues. *Nat Rev Cancer.* 2018;18(1):51–63.

776 13. Piazzi M, et al. Signal transduction in ribosome biogenesis: a recipe to avoid
777 disaster. *Int J Mol Sci.* 2019;20(11).

778 14. Potapova TA, and Gerton JL. Ribosomal DNA and the nucleolus in the context
779 of genome organization. *Chromosome Res.* 2019;27(1-2):109–27.

780 15. Moss T, et al. The chromatin landscape of the ribosomal RNA genes in mouse
781 and human. *Chromosome Res.* 2019;27(1-2):31–40.

782 16. Zhang Y, and Lu H. Signaling to p53: ribosomal proteins find their way. *Cancer*
783 *Cell.* 2009;16(5):369–77.

784 17. Yang K, et al. Nucleolar Stress: hallmarks, sensing mechanism and diseases.
785 *Cell Stress.* 2018;2(6):125–40.

786 18. Nicolas E, et al. Involvement of human ribosomal proteins in nucleolar structure
787 and p53-dependent nucleolar stress. *Nat Commun.* 2016;7:11390.

788 19. Ariyoshi M, and Schwabe JW. A conserved structural motif reveals the essential
789 transcriptional repression function of Spen proteins and their role in
790 developmental signaling. *Genes Dev.* 2003;17(15):1909–20.

791 20. Arieti F, et al. The crystal structure of the Split End protein SHARP adds a new
792 layer of complexity to proteins containing RNA recognition motifs. *Nucleic*

793 *Acids Res.* 2014;42(10):6742–52.

794 21. Shi Y, et al. Sharp, an inducible cofactor that integrates nuclear receptor
795 repression and activation. *Genes Dev.* 2001;15(9):1140–51.

796 22. Kuroda K, et al. Regulation of marginal zone B cell development by MINT, a
797 suppressor of Notch/RBP-J signaling pathway. *Immunity.* 2003;18(2):301–12.

798 23. Boeren J, and Gribnau J. Xist-mediated chromatin changes that establish
799 silencing of an entire X chromosome in mammals. *Curr Opin Cell Biol.*
800 2021;70:44–50.

801 24. Dossin F, et al. SPEN integrates transcriptional and epigenetic control of X-
802 inactivation. *Nature.* 2020;578(7795):455–60.

803 25. Yao H, et al. Mediation of CTCF transcriptional insulation by DEAD-box RNA-
804 binding protein p68 and steroid receptor RNA activator SRA. *Genes Dev.*
805 2010;24(22):2543–55.

806 26. Carter AC, et al. Spen links RNA-mediated endogenous retrovirus silencing and
807 X chromosome inactivation. *Elife.* 2020;9.

808 27. Drygin D, et al. Targeting RNA polymerase I with an oral small molecule CX-
809 5461 inhibits ribosomal RNA synthesis and solid tumor growth. *Cancer Res.*
810 2011;71(4):1418–30.

811 28. Bywater MJ, et al. Inhibition of RNA polymerase I as a therapeutic strategy to
812 promote cancer-specific activation of p53. *Cancer Cell.* 2012;22(1):51–65.

813 29. Khot A, et al. First-in-Human RNA Polymerase I Transcription Inhibitor CX-
814 5461 in Patients with Advanced Hematologic Cancers: Results of a Phase I

815 Dose-Escalation Study. *Cancer Discov.* 2019;9(8):1036–49.

816 30. Sanij E, et al. CX-5461 activates the DNA damage response and demonstrates
817 therapeutic efficacy in high-grade serous ovarian cancer. *Nat Commun.*
818 2020;11(1):2641.

819 31. Yabe D, et al. Generation of a conditional knockout allele for mammalian Spen
820 protein Mint/SHARP. *Genesis.* 2007;45(5):300–6.

821 32. Bieging KT, et al. Unravelling mechanisms of p53-mediated tumour
822 suppression. *Nat Rev Cancer.* 2014;14(5):359–70.

823 33. Geyer RK, et al. The MDM2 RING-finger domain is required to promote p53
824 nuclear export. *Nat Cell Biol.* 2000;2(9):569–73.

825 34. ElSawy KM, et al. A spatiotemporal characterization of the effect of p53
826 phosphorylation on its interaction with MDM2. *Cell Cycle.* 2015;14(2):179–88.

827 35 Liu Y, et al. p53 modifications: exquisite decorations of the powerful guardian.
828 *J Mol Cell Biol.* 2019;11(7):564–77.

829 36. Mantovani F, et al. Interaction of p53 with prolyl isomerases: Healthy and
830 unhealthy relationships. *Biochim Biophys Acta.* 2015;1850(10):2048–60.

831 37 Jeong K, et al. p53 negatively regulates Pin1 expression under ER stress.
832 *Biochem Biophys Res Commun.* 2014;454(4):518–23.

833 38. Lafontaine DLJ, et al. The nucleolus as a multiphase liquid condensate. *Nat Rev*
834 *Mol Cell Biol.* 2021;22(3):165–82.

835 39. Wang X, et al. Mutual dependency between lncRNA LETN and protein NPM1
836 in controlling the nucleolar structure and functions sustaining cell proliferation.

837 *Cell Res.* 2021;31(6):664–83.

838 40. Zentner GE, et al. Integrative genomic analysis of human ribosomal DNA.
839 *Nucleic Acids Res.* 2011;39(12):4949–60.

840 41. Herdman C, et al. A unique enhancer boundary complex on the mouse ribosomal
841 RNA genes persists after loss of Rrn3 or UBF and the inactivation of RNA
842 polymerase I transcription. *PLoS Genet.* 2017;13(7):e1006899.

843 42. Mars JC, et al. A deconvolution protocol for ChIP-seq reveals analogous
844 enhancer structures on the mouse and human ribosomal RNA genes. *G3*
845 *(Bethesda).* 2018;8(1):303–14.

846 43. Hamdane N, et al. Conditional inactivation of upstream binding factor reveals
847 its epigenetic functions and the existence of a somatic nucleolar precursor body.
848 *PLoS Genet.* 2014;10(8):e1004505.

849 44. Huang K, et al. Ribosomal RNA gene transcription mediated by the master
850 genome regulator protein CCCTC-binding factor (CTCF) is negatively
851 regulated by the condensin complex. *J Biol Chem.* 2013;288(36):26067–77.

852 45. van de Nobelen S, et al. CTCF regulates the local epigenetic state of ribosomal
853 DNA repeats. *Epigenetics Chromatin.* 2010;3(1):19.

854 46. Mayer C, et al. Intergenic transcripts regulate the epigenetic state of rRNA genes.
855 *Mol Cell.* 2006;22(3):351–61.

856 47. Bierhoff H, et al. Noncoding transcripts in sense and antisense orientation
857 regulate the epigenetic state of ribosomal RNA genes. *Cold Spring Harb Symp*
858 *Quant Biol.* 2010;75:357–64.

859 48. Zhao Z, et al. lncRNA PAPAS tethered to the rDNA enhancer recruits
860 hypophosphorylated CHD4/NuRD to repress rRNA synthesis at elevated
861 temperatures. *Genes Dev.* 2018;32(11-12):836–48.
862 49. Abraham KJ, et al. Nucleolar RNA polymerase II drives ribosome biogenesis.
863 *Nature.* 2020;585(7824):298–302.
864 50. Vydzhak O, et al. Non-coding RNAs at the eukaryotic rDNA locus: RNA-DNA
865 hybrids and beyond. *J Mol Biol.* 2020;432(15):4287–304.
866 51. Leite de Oliveira R, et al. Gene-targeting of Phd2 improves tumor response to
867 chemotherapy and prevents side-toxicity. *Cancer Cell.* 2012;22(2):263–77.
868 52. Zhang N, et al. DLL1 orchestrates CD8(+) T cells to induce long-term vascular
869 normalization and tumor regression. *Proc Natl Acad Sci U S A.* 2021;118(22):
870 e2020057118.
871 53. Han H, et al. Inducible gene knockout of transcription factor recombination
872 signal binding protein-J reveals its essential role in T versus B lineage decision.
873 *Int Immunol.* 2002;14(6):637–45.
874 54. Reschke M, et al. Nucleic acid delivery to the vascular endothelium. *Mol Pharm.*
875 2022;19(12):4466–86.
876 55. Sakurai Y, et al. RNAi-mediated gene knockdown and anti-angiogenic therapy
877 of RCCs using a cyclic RGD-modified liposomal-siRNA system. *J Control*
878 *Release.* 2014;173:110–8.
879 56. Ye Q, et al. Therapeutic targeting of RNA polymerase I with the small-molecule
880 CX-5461 for prevention of arterial injury-induced neointimal hyperplasia.

881 *Arterioscler Thromb Vasc Biol.* 2017;37(3):476–484.

882 57. Men H, et al. The regulatory roles of p53 in cardiovascular health and disease.
883 *Cell Mol Life Sci.* 2021;78(5):2001–18.

884 58. Warboys CM, et al. Disturbed flow promotes endothelial senescence via a p53-
885 dependent pathway. *Arterioscler Thromb Vasc Biol.* 2014;34(5):985–95.

886 59. Teodoro JG, et al. Inhibition of tumor angiogenesis by p53: a new role for the
887 guardian of the genome. *J Mol Med (Berl).* 2007;85(11):1175–86.

888 60. Stone OA, et al. Loss of pyruvate kinase M2 limits growth and triggers innate
889 immune signaling in endothelial cells. *Nat Commun.* 2018;9(1):4077.

890 61. Kim B, et al. Endothelial pyruvate kinase M2 maintains vascular integrity. *J*
891 *Clin Invest.* 2018;128(10):4543–56.

892 62. Van der Veldt AA, et al. Rapid decrease in delivery of chemotherapy to tumors
893 after anti-VEGF therapy: implications for scheduling of anti-angiogenic drugs.
894 *Cancer Cell.* 2012;21(1):82–91.

895 63. Schaaf MB, et al. Autophagy in endothelial cells and tumor angiogenesis. *Cell*
896 *Death Differ.* 2019;26(4):665–79.

897 64. Lloyd AC. The regulation of cell size. *Cell.* 2013;154(6):1194–205.

898 65. Pan M, et al. The chemotherapeutic CX-5461 primarily targets TOP2B and
899 exhibits selective activity in high-risk neuroblastoma. *Nat Commun.*
900 2021;12(1):6468.

901 66. Bergeron-Sandoval LP, et al. Mechanisms and consequences of macromolecular
902 phase separation. *Cell.* 2016;165(5):1067–79.

903 67. Jin LH, et al. Requirement of Split ends for epigenetic regulation of Notch
904 signal-dependent genes during infection-induced hemocyte differentiation. *Mol*
905 *Cell Biol.* 2009;29(6):1515–25.
906 68. Girard V, et al. Spen modulates lipid droplet content in adult Drosophila glial
907 cells and protects against paraquat toxicity. *Sci Rep.* 2020;10(1):20023.
908 69. Wang Y, et al. Ephrin-B2 controls VEGF-induced angiogenesis and
909 lymphangiogenesis. *Nature.* 2010;465(7297):483–6.
910 70. Maeder ML, et al. CRISPR RNA-guided activation of endogenous human genes.
911 *Nat Methods.* 2013;10(10):977–9.
912 71. Leone S, et al. The RNA helicase DHX9 establishes nucleolar heterochromatin,
913 and this activity is required for embryonic stem cell differentiation. *EMBO Rep.*
914 2017;18(7):1248–62.
915 72. Santoro R, et al. Intergenic transcripts originating from a subclass of ribosomal
916 DNA repeats silence ribosomal RNA genes in trans. *EMBO Rep.*
917 2010;11(1):52–8.
918 73. GENE DENOVO Biotechnology. OmicShare Tools.
919 https://www.omicshare.com/tools.
920 74. Donati G, et al. 5S ribosomal RNA is an essential component of a nascent
921 ribosomal precursor complex that regulates the Hdm2-p53 checkpoint. *Cell Rep.*
922 2013;4(1):87–98.
923
924

Figure legends

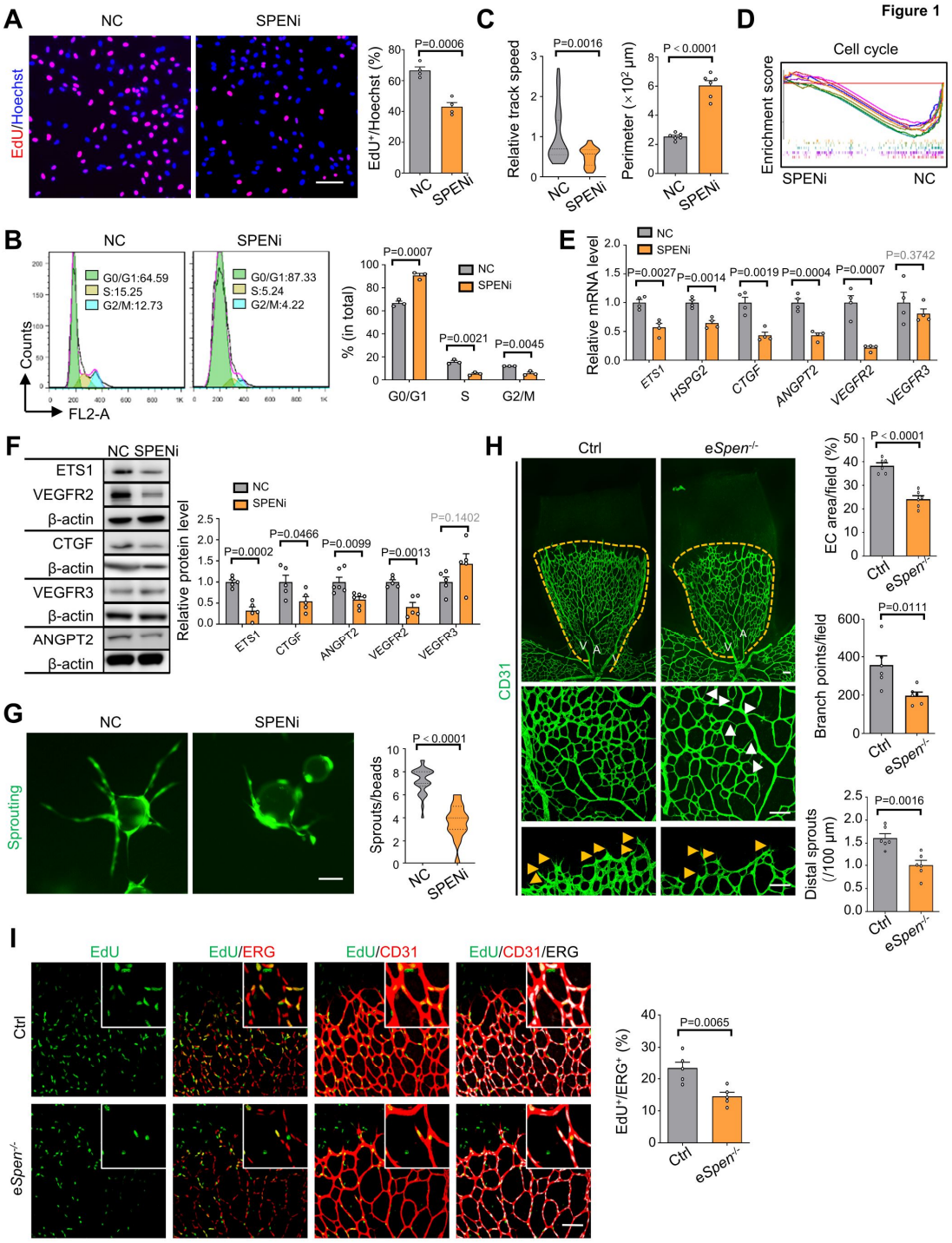

Figure 1. Endothelial SPEN deficiency represses EC proliferation and blunts angiogenesis. (**A–C**) HUVECs were transduced with NC or SPENi lentivirus expressing EGFP. Cell proliferation was determined by EdU incorporation (**A**) (n = 4)

930 and cell cycle analysis (**B**) (n = 3). In (**C**), ECs were recorded with a living cell imaging
931 workstation (Supplemental Figure 1F and Supplemental Video, 1 and 2), and the
932 relative track speed of cells (n = 35 and 21 cell tracks for NC and SPENi, respectively)
933 and cell perimeters (n = 6) were compared. Scale bars, 100 μm. (**D**) HUVECs were
934 transduced with NC or SPENi lentivirus and subjected to RNA-seq (n = 4). Cell cycle-
935 related gene sets were analysed by GSEA (color-coded gene sets are listed in
936 Supplemental Figure 1H). (**E** and **F**) HUVECs were transduced with NC or SPENi
937 lentivirus. The expression of angiogenesis-related genes was determined by RT–qPCR
938 (**E**) (n = 4) and immunoblotting (**F**) (n = 5 except for n = 6 for ANGPT blots, and the
939 β-actin of each blot was shown). Scale bar, 100 μm. (**G**) Sprouting was assessed by the
940 microbead sprouting assay and quantitatively compared (n = 30 beads from 3 biological
941 replicates). Scale bar, 100 μm. (**H**) The retinal vasculature of P6 pups was stained with
942 anti-CD31 and photographed. The middle and lower panels show the remodelling zone
943 and angiogenic frontier of retinas, respectively. A, artery; V, vein; white arrows, vessel
944 loops; yellow arrows, sprouts; yellow dashed lines, vascular radius. Scale bars, 100 μm.
945 The EC area (n = 6), branch number (n = 6), and distal sprouts (n = 6) were quantified.
946 (**I**) Immunostaining of mouse retinas after EdU labelling. EdU^+ ECs were compared (n
947 = 5). Scale bar, 100 μm. Data represent mean ± SEM; unpaired two-sided Student's t-
948 test.
949

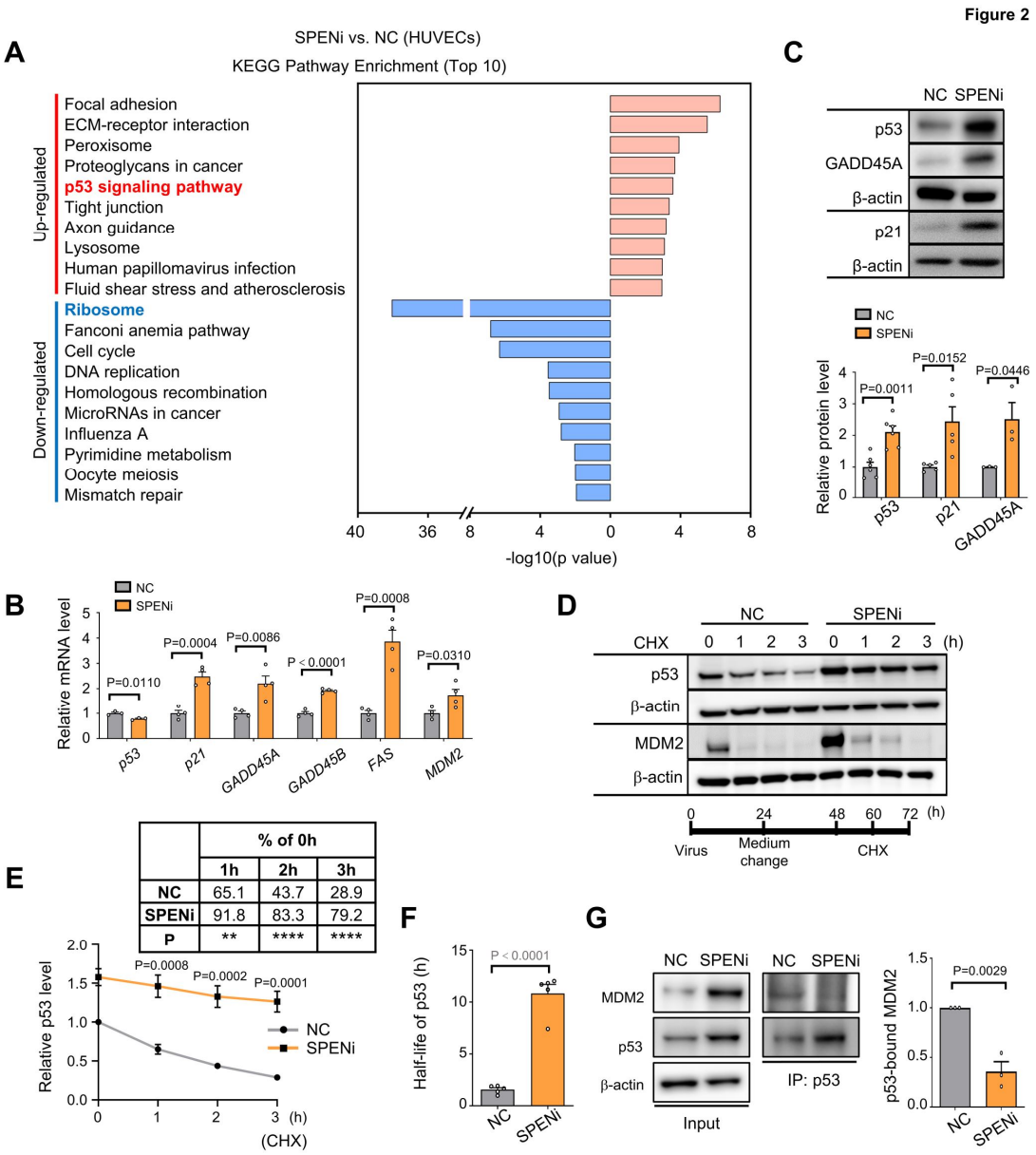

Figure 2. SPEN knockdown activates p53. (**A**) Signature genes that are differentially expressed in HUVECs transduced with NC or SPENi lentivirus, the top 10 markedly changed entries were presented. (**B** and **C**) HUVECs were transduced with NC or SPENi lentivirus. The expression of p53 and its downstream genes was determined by RT-qPCR (**B**) (n = 4, except for n = 3 in *p53*), and immunoblotting (**C**) (n = 6, 5, and 3 for p53, p21, and GADD45A, respectively, the β-actin of each blot was shown). (**D**–**F**) HUVECs were transduced with NC or SPENi lentivirus and cultured with CHX as

958 depicted. The p53 and MDM2 levels were assessed by immunoblotting at 0, 1, 2 and 3
959 h after CHX addition (n = 5, the β-actin of each blot was shown). The p53 level (**E**) and
960 its half-life (**F**) were determined. The inset table in (**E**) shows the percentage of p53
961 level at different time points vs p53 level of 0 h after CHX addition (**, $P < 0.01$; ****,
962 $P < 0.0001$). (**G**) HUVECs were transduced with NC or SPENi lentivirus. Cell extracts
963 were precipitated with anti-p53, and immunoblotted with anti-MDM2 (n = 3). Data
964 represent mean ± SEM; unpaired two-sided Student's t-test.
965

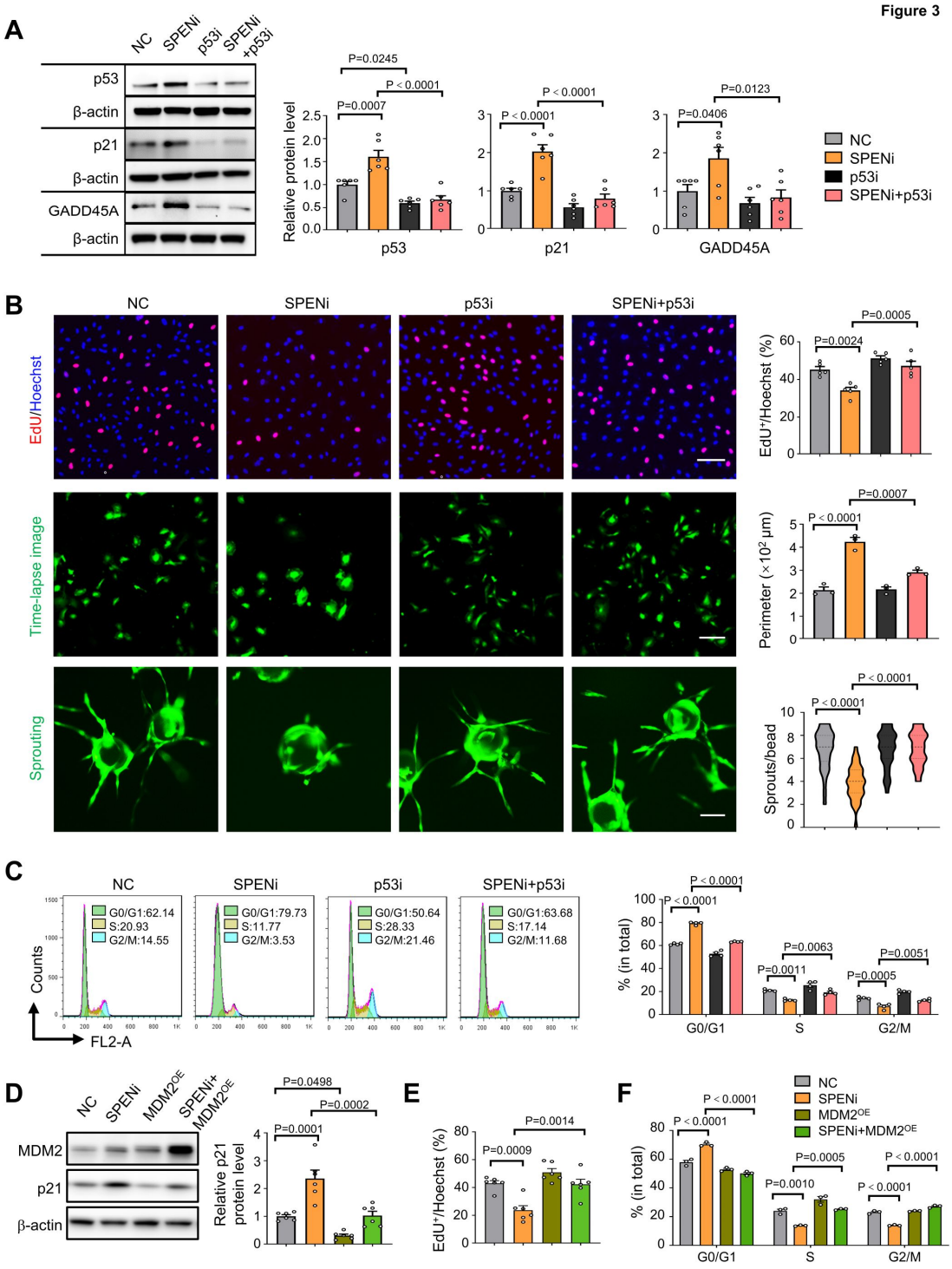

Figure 3. SPEN knockdown represses EC proliferation by activating p53. (**A**–**C**) HUVECs were transduced with NC, SPENi, p53i, or SPENi+p53i lentivirus expressing EGFP. The expression of p53, p21, and GADD45A was determined by immunoblotting (**A**) (n = 6, the β-actin of each blot was shown). The cell proliferation (n = 5), cell

971 perimeter (n = 3), and sprouts (n = 30 beads from 3 biological replicates) were
972 determined by the EdU incorporation, live cell imaging, and microbead sprouting assay,
973 respectively (**B**). The cell cycle progression was determined by FACS (**C**) (n = 4). Scale
974 bars, 100 μm. (**D**–**F**) HUVECs were transduced with SPENi or NC, and simultaneously
975 transduced with MDM2-overexpressing lentivirus. The p21 expression (**D**), cell
976 proliferation (**E**) and cell cycle progression (**F**) were determined (n = 6 for **D** and **E**, n
977 = 3 for **F**). Data represent mean ± SEM; one-way ANOVA with Tukey's multiple
978 comparisons test.
979

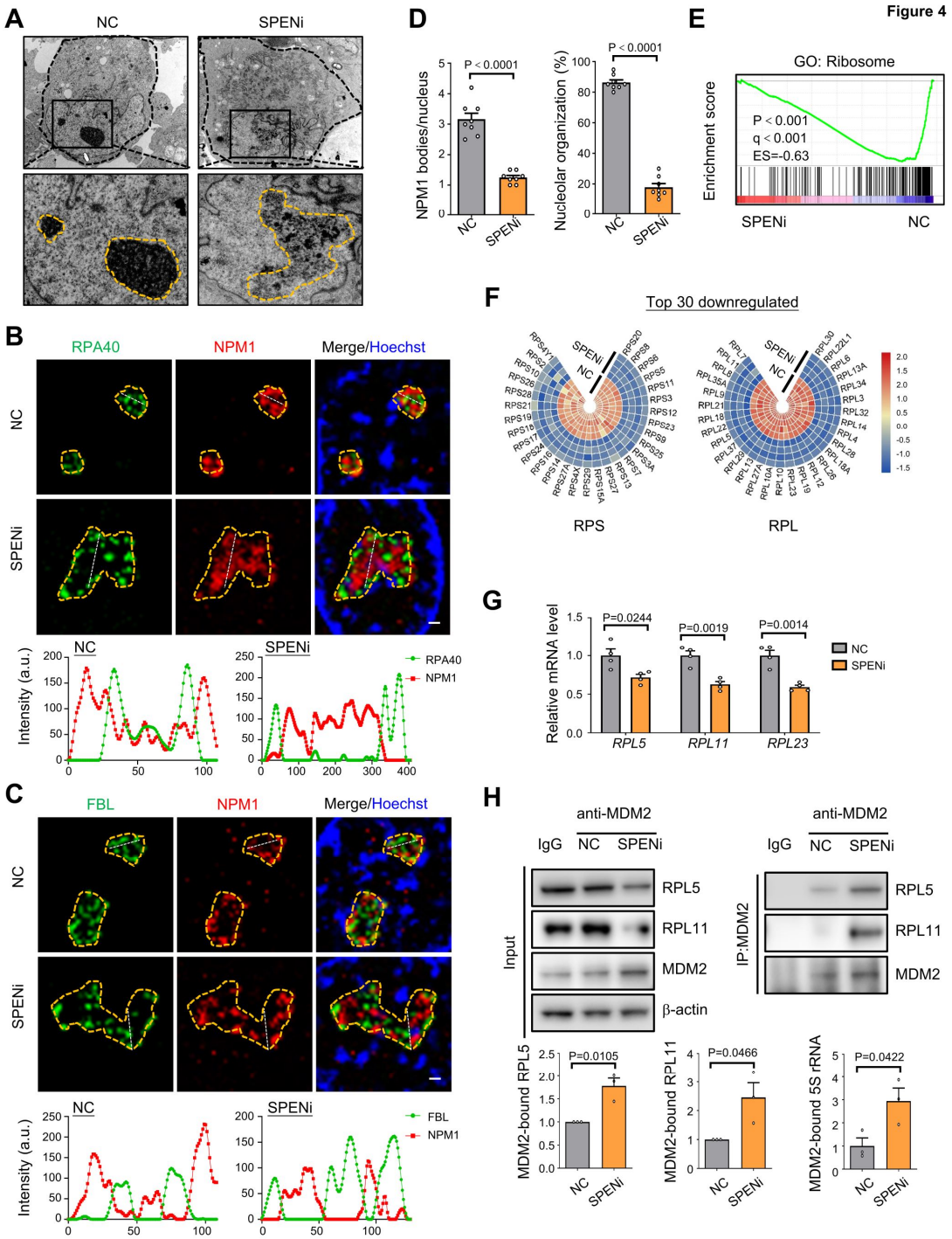

Figure 4. SPEN knockdown triggers nucleolar stress. (**A**) HUVECs were transduced with NC or SPENi lentivirus and observed under TEM. Dashed yellow lines, nucleoli. Scale bar, 1 μm. (**B**–**D**) HUVECs were transduced with NC or SPENi lentivirus and subjected to immunostaining followed by SIM microscopy. Dashed yellow lines,

985 nucleoli. The NPM1, UBF and RPA40 intensities along the white lines are plotted. The
986 NPM1 body number and HUVECs with normal nucleoli were counted (**D**) (n = 8).
987 Scale bar, 1 μm. (**E** and **F**) Analyses of ribosome-related genes by GSEA (**E**) and
988 Heatmaps (**F**) in HUVECs transduced with NC or SPENi lentivirus followed by RNA-
989 seq. (**G**) HUVECs were transduced with NC or SPENi lentivirus. The expression of
990 *RPL5*, *RPL11*, *RPL23* was determined by RT–qPCR (n = 4). (**H**) HUVECs were
991 transduced with NC or SPENi lentivirus. Cell lysates were immunoprecipitated with
992 anti-MDM2 after ultracentrifugation, and detected with anti-RPL5 and RPL11, or RT-
993 qPCR for 5S rRNA (n = 3). Data represent mean ± SEM; unpaired two-sided Student's
994 t-test.
995

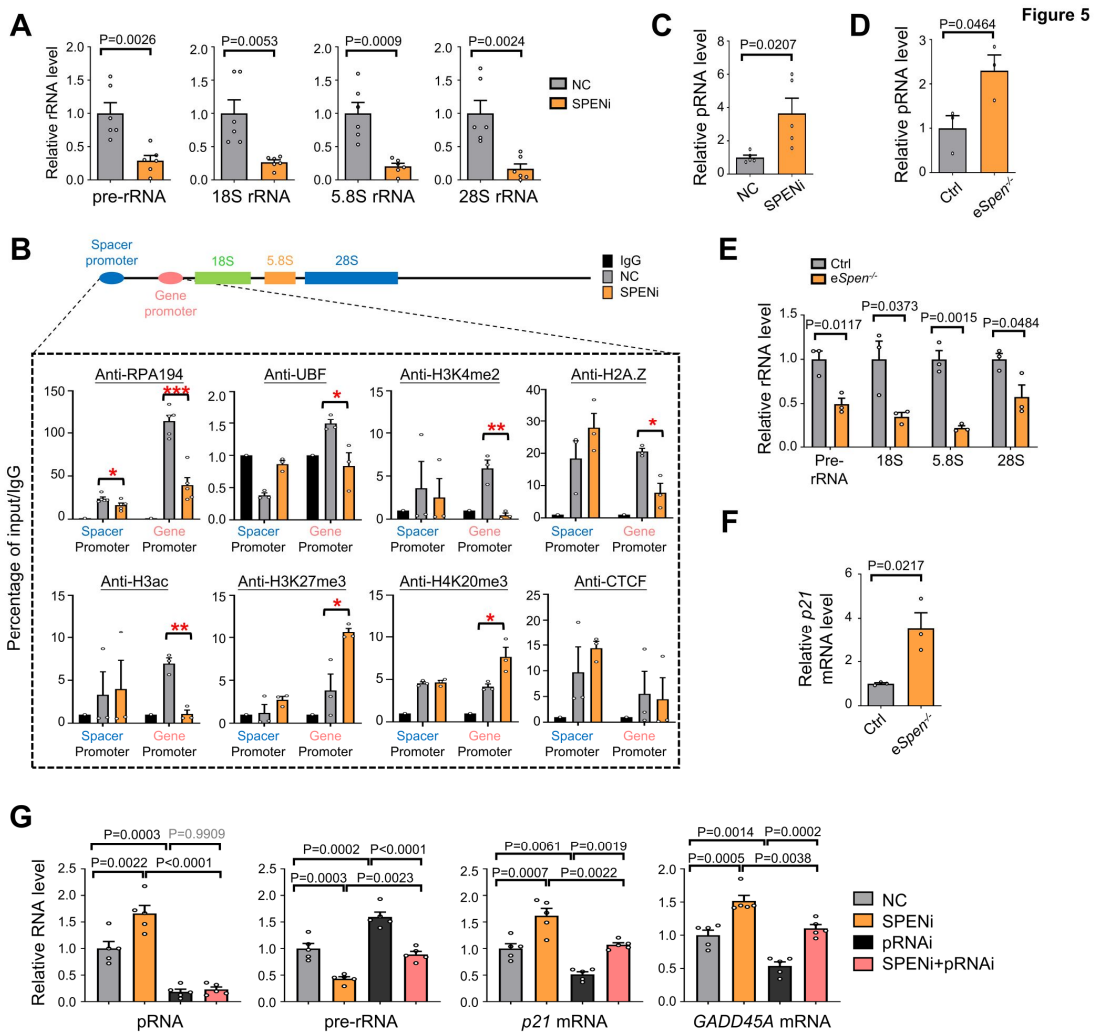

Figure 5. SPEN knockdown triggers nucleolar stress by upregulating pRNA in ECs. (**A**) HUVECs were transduced with NC or SPENi lentivirus. The expression of pre-rRNA, 18S, 5.8S, and 28S rRNA was determined by RT–qPCR (n = 6). (**B**) HUVECs were transduced with NC or SPENi lentivirus. ChIP-qPCR was performed with anti-RPA194, anti-UBF, anti-H3K4me2, anti-H2A.Z, anti-H3ac, anti-H3K27me3, anti-H4K20me3, and anti-CTCF antibodies (n = 3, except for n = 5 in anti-RPA194). *, $P < 0.05$, **, $P < 0.01$, ***, $P < 0.001$. (**C**) HUVECs were transduced with NC or SPENi lentivirus. pRNA expression was determined by strand-specific RT–qPCR (n = 5). (**D-F**) ECs from P6 retinas of e*Spen*$^{-/-}$ and control mice were analyzed by RT-qPCR for the

1006 expression of pRNA (**D**), pre-rRNA and mature rRNAs (**E**), and *p21* (**F**) (n = 3, each
1007 sample is a pool of 3–4 retinas). (**G**) HUVECs were transduced with lentivirus as
1008 indicated. The expression of pRNA, pre-rRNA, *p21*, and *GADD45A* was determined
1009 by RT–qPCR (n = 5). Data represent mean ± SEM; one-way ANOVA with Tukey's
1010 multiple comparisons test in (**G**), and unpaired two-sided Student's t-test for others.
1011

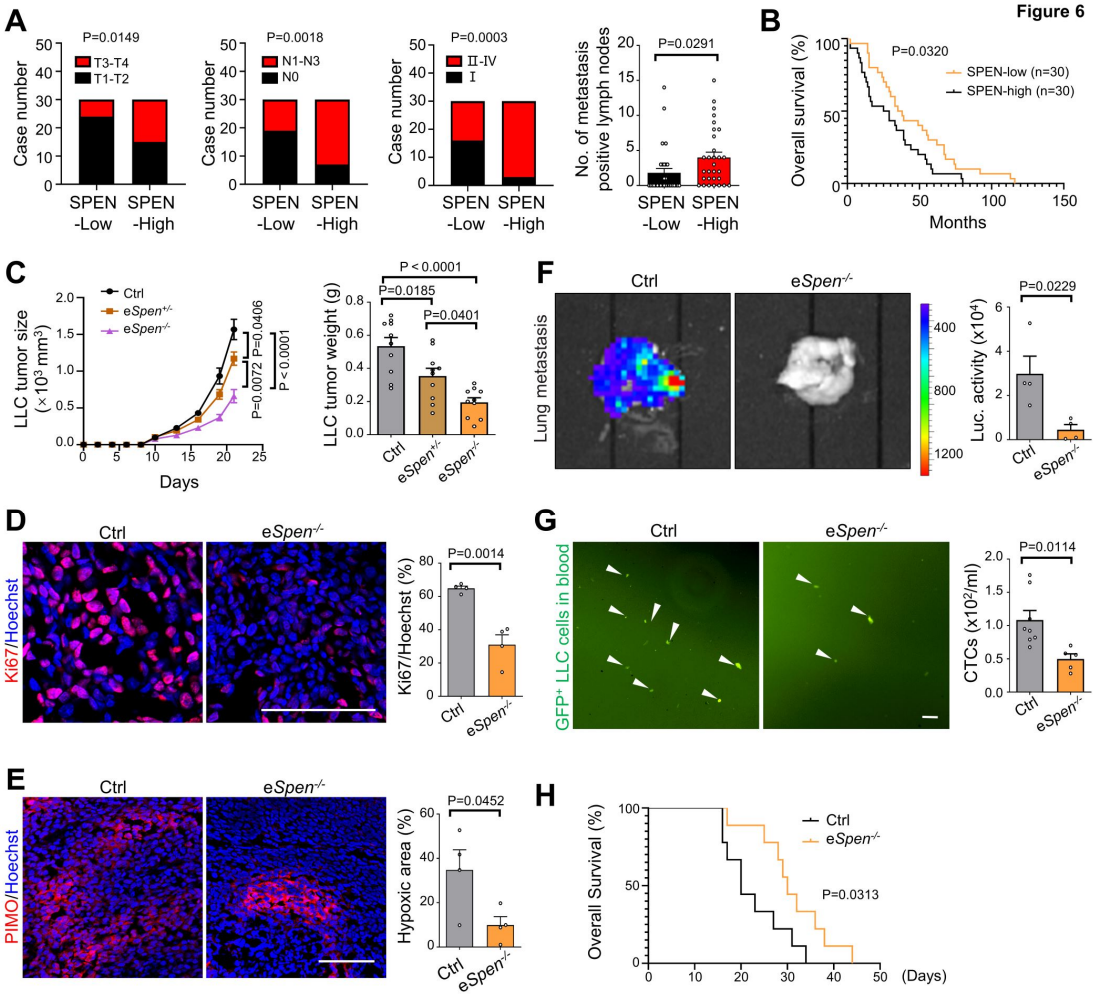

1012

1013 **Figure 6. Endothelial *Spen* ablation represses tumor growth.** (**A** and **B**) Human lung

1014 cancer biopsies were immunostained for CD31 and SPEN, and the SPEN intensity in

1015 the CD31^{+} area was quantified. Tumor progression was analysed between the

1016 endothelial SPEN-high and SPEN-low groups (**A**). The correlation of endothelial SPEN

1017 level with overall survival was evaluated by the Kaplan–Meier analysis (**B**). n = 30

1018 patients per group. (**C**) Mice were inoculated with LLC cells. Tumor size was monitored

1019 and tumor weight was compared on 21 dpi (n = 10). (**D** and **E**) Ctrl and e*Spen*$^{-/-}$ mice

1020 were inoculated with LLC. Tumors of 21 dpi were immunostained with Ki67 and

1021 quantitatively compared (**D**) (n = 4). Tumor hypoxia was evaluated by staining with

1022 Hypoxyprobe (**E**) (n = 4). Scale bars, 100 μm. (**F**) Mice were inoculated with luciferase^{+}
1023 LLC cells. Tumors were removed on 14 dpi, and the mice were maintained for
1024 additional 28 days. Lung metastasis was evaluated using chemoluminescence (n = 4).
1025 (**G**) Mice were inoculated with GFP^{+} LLC cells. Circulating GFP^{+} LLC cells in blood
1026 were counted on 21 dpi (n = 8 and 5 for Ctrl and e*Spen*$^{-/-}$, respectively). Scale bar,
1027 100 μm. (**H**) Mice were inoculated with LLC cells. Tumors were removed on 21 dpi,
1028 and mouse survival was plotted thereafter (n = 9). Data represent mean ± SEM; log-
1029 rank (Mantel-Cox) test in (**B** and **H**), one-way ANOVA with Tukey's multiple
1030 comparisons test in (**C**), chi-square χ^2 analyses in (**A**) except for lymph node metastasis,
1031 and unpaired two-sided Student's t-test for others.
1032

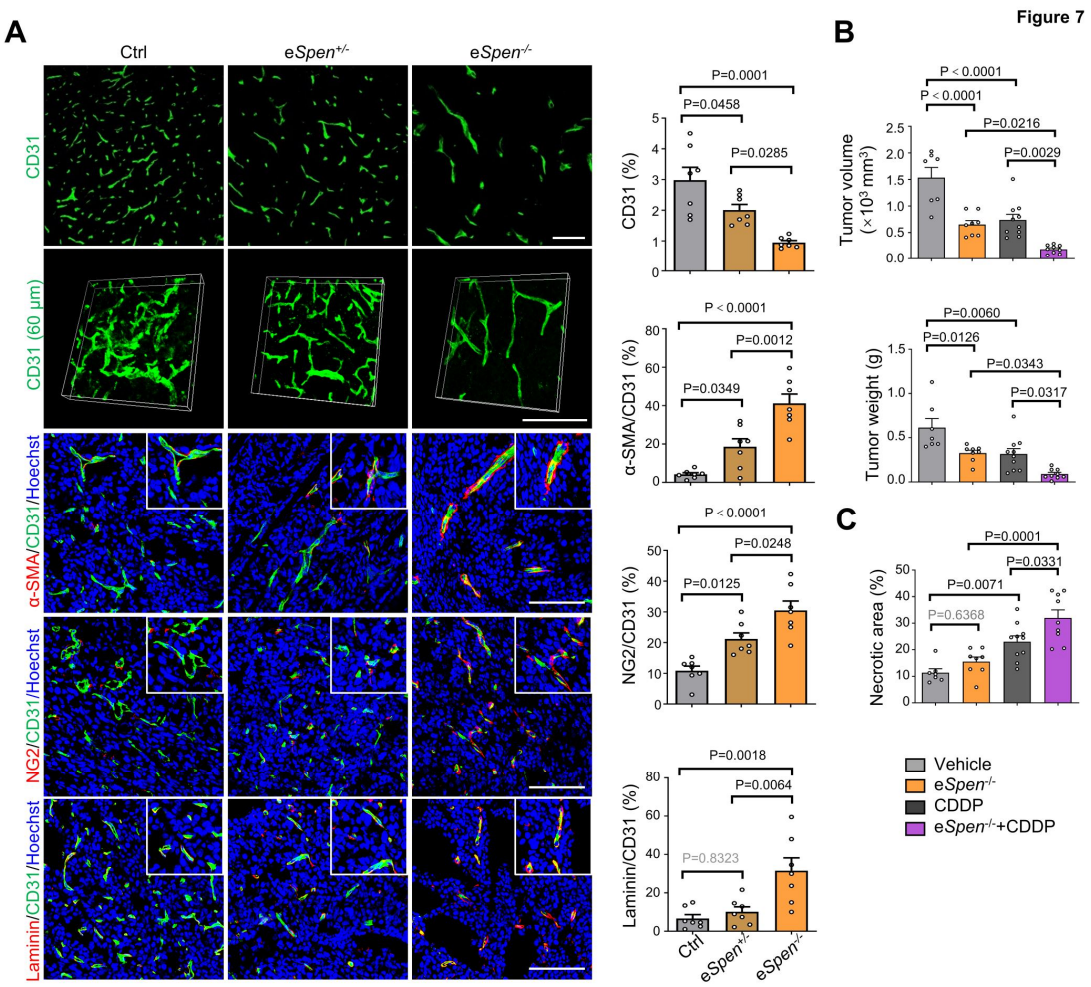

Figure 7. Endothelial *Spen* ablation induces tumor vessel normalization. (**A**) LLC tumors from Ctrl, e*Spen*$^{+/-}$, and e*Spen*$^{-/-}$ mice were stained for CD31, α-SMA, NG2, and laminin by immunofluorescence on 21 dpi. CD31^{+}, α-SMA^{+}CD31^{+}, NG2^{+}CD31^{+}, and laminin^{+}CD31^{+} areas were quantitatively compared (n = 7). The CD31 immunofluorescence (60 μm thickness) was used to reconstruct tumor vessels (representing 3 independent experiments). Scale bars, 100 μm. (**B** and **C**) Mice bearing LLC tumors were treated with CDDP from 7 dpi. Tumor size and weight were evaluated on 21 dpi (**B**), and tumor sections were stained with H&E (Supplemental Figure 7D), and necrosis areas were determined (**C**) (n = 7, 8, 10 and 9 for Ctrl, e*Spen*$^{-/-}$, CDDP and e*Spen*$^{-/-}$+CDDP, respectively). Data represent mean ± SEM; one-way ANOVA with

Tukey's multiple comparisons test.

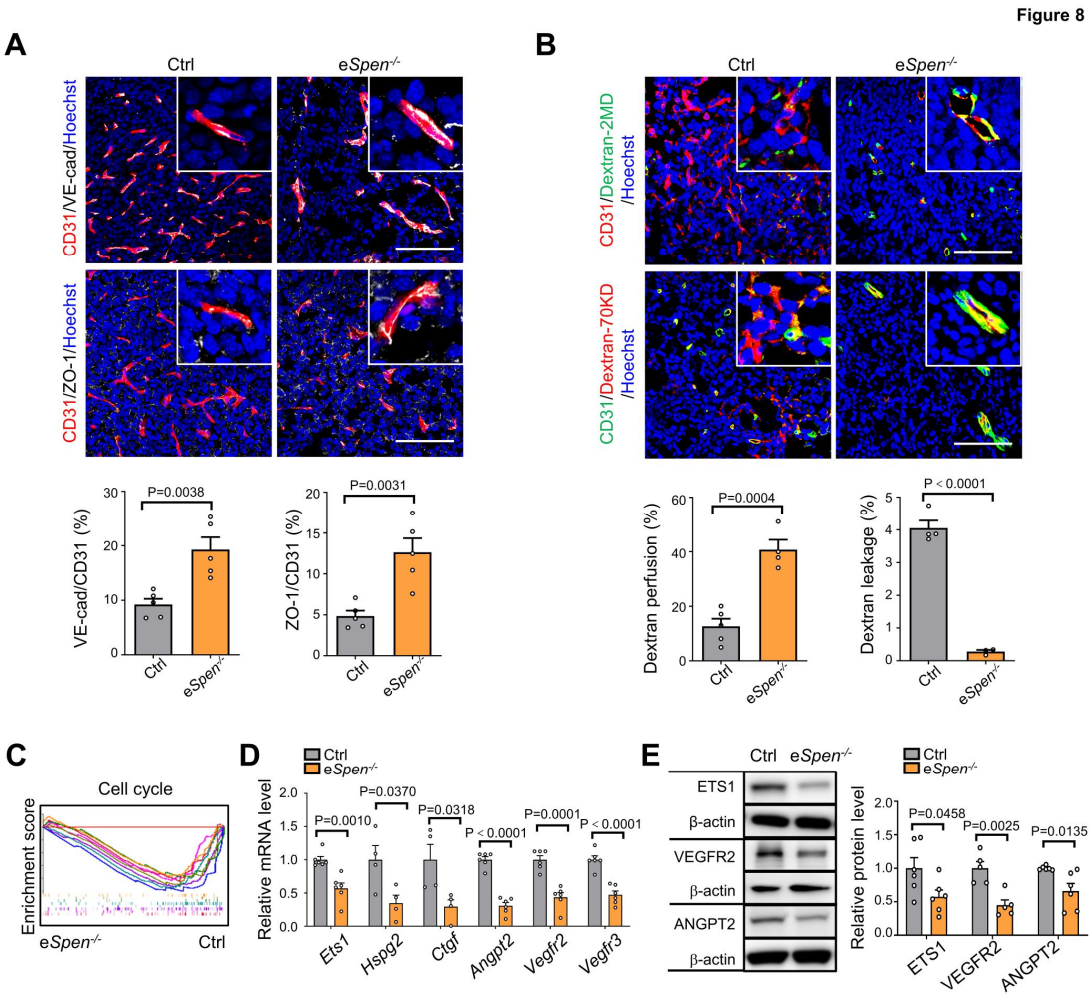

Figure 8. Endothelial *Spen* ablation normalizes functionally tumor vessels. (**A**) LLC tumor sections from Ctrl and e*Spen*$^{-/-}$ mice were stained by CD31 and VE-cadherin or CD31 and ZO-1 immunofluorescence, and quantitatively compared (n = 5). Scale bars, 100 μm. (**B**) Vessel perfusion and leakage in tumors were determined with FITC-Dextran-2MD (n = 5 and 4 for Ctrl and e*Spen*$^{-/-}$, respectively) or Texas Red-Dextran-70KD (n = 4 and 3 for Ctrl and e*Spen*$^{-/-}$, respectively). Scale bars, 100 μm. (**C**) Ctrl and e*Spen*$^{-/-}$ TECs were subjected to RNA-seq. Cell cycle-associated genesets were analysed by GSEA (color-coded gene sets are listed in Supplemental Figure 1H). (**D** and **E**) Expression of angiogenesis-related genes in TECs was determined by RT-qPCR (**D**) (n = 4) or immunoblotting (**E**) (n = 6 except for n = 5 for VEGFR2; the β-actin of

1057 each blot was shown). Data represent mean ± SEM; unpaired two-sided Student's t-test

1058 in others.

1059

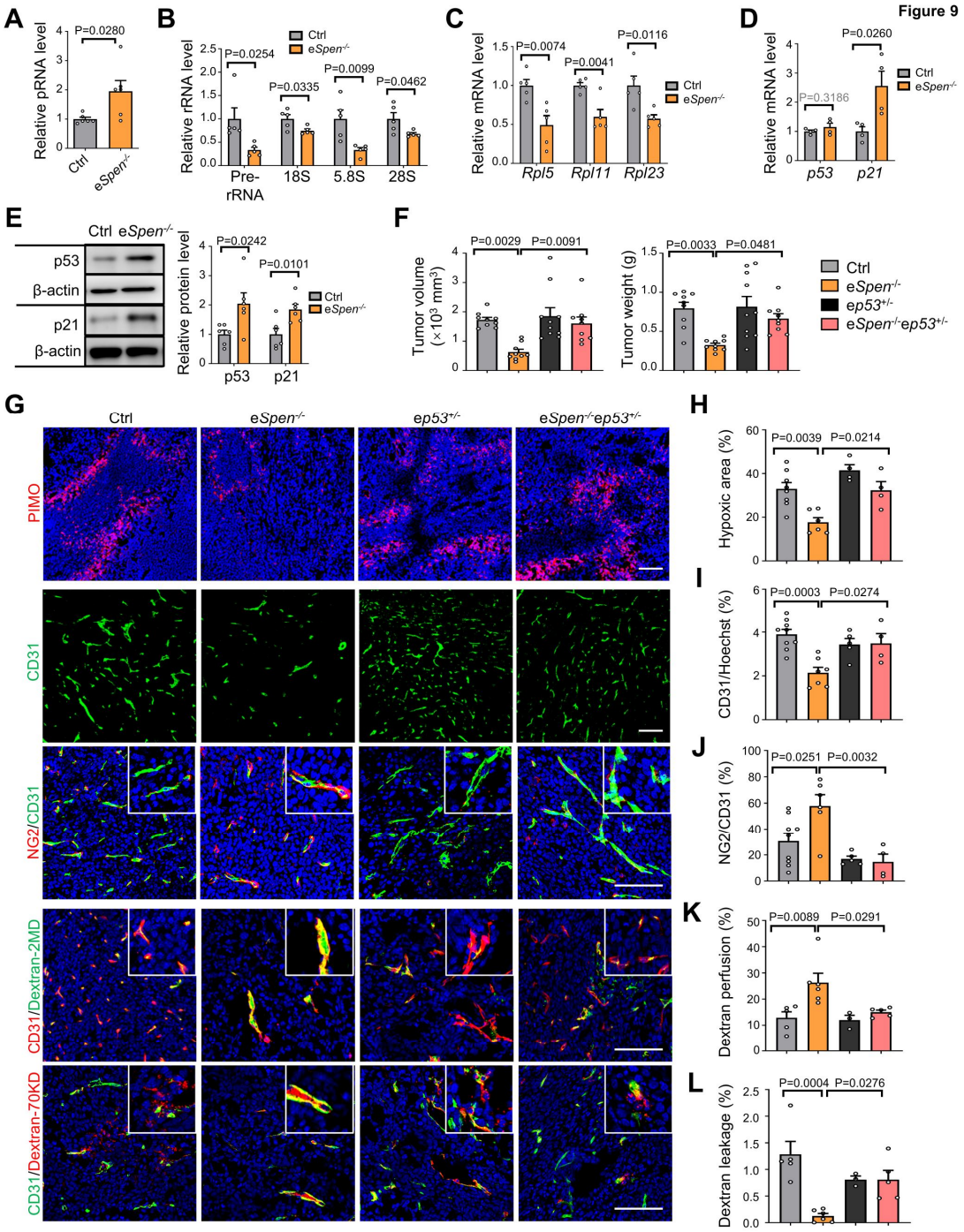

Figure 9. *Spen* ablation-mediated tumor vessel normalization requires p53. (**A**) pRNA expression in TECs as determined by strand-specific RT–qPCR (n = 6). (**B** and **C**) Expression of pre-rRNA, 18S, 5.8S, and 28S rRNAs (**B**), as well as *Rpl5*, *Rpl11*, and *Rpl23* (**C**) in TECs was determined by RT–qPCR (n = 5). (**D** and **E**) Expression of *p53* and *p21* in TECs was determined by RT-qPCR (**D**) (n = 4) and immunoblotting (**E**)

1066 (n = 6, the β-actin of each blot was shown). (**F**) Mice with different genotypes were
1067 inoculated with LLC. Tumors were dissected on 21 dpi (Supplemental Figure 8E).
1068 Tumor size and weight were quantified (n = 9, 9, 10 and 9 for Ctrl, e*Spen*$^{-/-}$, e*p53*$^{+/-}$, and
1069 e*Spen*$^{-/-}$e*p53*$^{+/-}$, respectively). (**G**–**L**) LLC tumors of 21 dpi were stained with
1070 Hypoxyprobe, immunofluorescence, or assayed for vessel perfusion and leakage with
1071 FITC-Dextran-2MD or Texas Red-Dextran-70KD (**G**). The hypoxia (**H**) (n = 8, 6, 4
1072 and 4 for Ctrl, e*Spen*$^{-/-}$, e*p53*$^{+/-}$, and e*Spen*$^{-/-}$e*p53*$^{+/-}$, respectively), vessel density
1073 (CD31^{+}) (**I**) (n = 9, 7, 5 and 4 for Ctrl, e*Spen*$^{-/-}$, e*p53*$^{+/-}$, and e*Spen*$^{-/-}$e*p53*$^{+/-}$, respectively),
1074 pericyte coverage (CD31^{+}NG2^{+}) (**J**) (n = 9, 6, 5 and 4 for Ctrl, e*Spen*$^{-/-}$, e*p53*$^{+/-}$, and
1075 e*Spen*$^{-/-}$e*p53*$^{+/-}$, respectively), as well as vessel perfusion (**K**) and leakage (**L**) (n = 5, 6,
1076 3 and 5 for Ctrl, e*Spen*$^{-/-}$, e*p53*$^{+/-}$, and e*Spen*$^{-/-}$e*p53*$^{+/-}$, respectively), were quantified.
1077 Scale bar, 100 μm. Data represent mean ± SEM; unpaired two-sided Student's t-test in
1078 (**A**–**E**); one-way ANOVA with Tukey's multiple comparisons test in (**F**, **H**–**L**).
1079

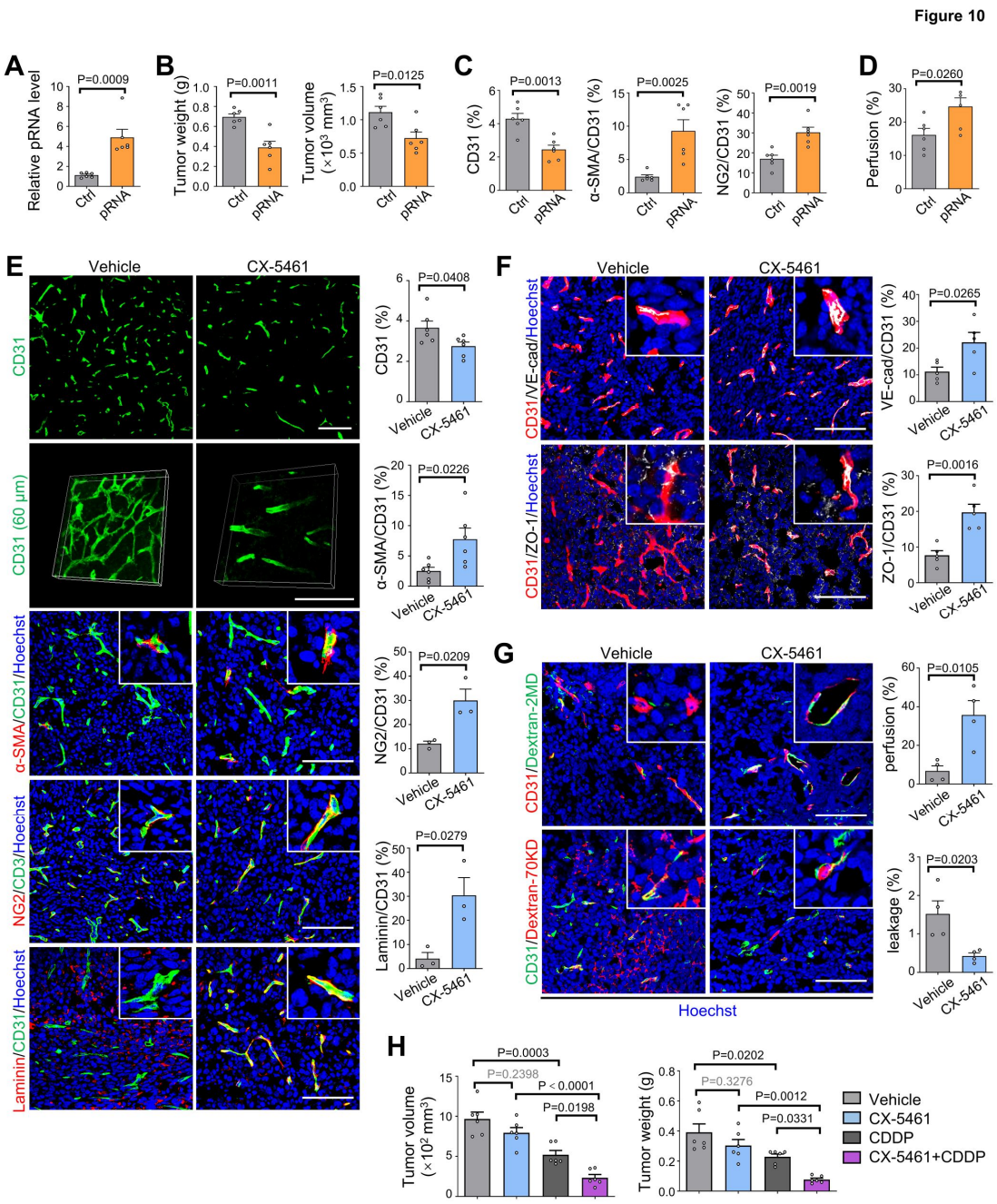

Figure 10. An RNPI inhibitor induces tumor vessel normalization and enhances efficacy of cisplatin. (**A**–**D**) Mice were inoculated with LLC and injected with LNP-pRNA or LNP-Ctrl i.v every three days from 7 to 21 dpi. pRNA expression in TECs was determined by RT-qPCR (**A**). Tumor growth was determined (**B**). Tumor vessels were stained with immunofluorescence, and vessel perfusion was evaluated (**C** and **D**) (Supplemental Figure 9F–9H) (n = 6). (**E**) Mice were inoculated with LLC and orally

1087 administered with 50 mg/kg CX-5461 every two days from 7 to 14 dpi. Tumor sections
1088 were immunostained on 14 dpi with anti-CD31 (n = 6), anti-CD31 plus anti-α-SMA (n
1089 = 6), anti-CD31 plus anti-NG2 (n = 3), and anti-CD31 plus anti-laminin (n = 3). Tumor
1090 vessels were reconstructed with CD31 immunofluorescence (60 μm thickness)
1091 (representing 3 independent experiments). Scale bars, 100 μm. (**F**) LLC tumor sections
1092 from mice treated with CX-5461 were stained by CD31 and VE-cadherin or CD31 and
1093 ZO-1 immunofluorescence, and quantitatively compared (n = 5). Scale bars, 100 μm.
1094 (**G**) Vessel perfusion and leakage were assessed (n = 4). Scale bars, 100 μm. (**H**) Mice
1095 bearing LLC tumors were orally administered 50 mg/kg CX-5461 every two days and
1096 injected i.p with CDDP every three days from 7 to 14 dpi. Tumors were dissected
1097 (Supplemental Figure 10D), and tumor sizes and weights were compared (n = 6). Data
1098 represent mean ± SEM; one-way ANOVA with Tukey's multiple comparisons test in
1099 (**H**), and unpaired two-sided Student's t-test for others.